THE ASTROPHYSICAL JOURNAL, 489:175–198, 1997 November 1

THE IDENTIFICATION OF TWO DIFFERENT SPECTRAL TYPES OF PULSES IN GAMMA-RAY BURSTS

G. N. PENDLETON, W. S. PACIESAS, M. S. BRIGGS, R. D. PREECE, AND R. S. MALLOZZI
Department of Physics, University of Alabama in Huntsville, Huntsville, AL 35899

C. A. MEEGAN, J. M. HORACK, AND G. J. FISHMAN
NASA/Marshall Space Flight Center, Huntsville, AL 35812

D. L. BAND, J. L. MATTESON, AND R. T. SKELTON
CASS0111, University of California, San Diego, La Jolla, CA 92093

J. HAKKILA
Department of Physics and Astronomy, Mankato State University, Mankato, MN 56002-8400

L. A. FORD
Department of Physics and Astronomy, University of Wisconsin, Eau Claire, P.O. Box 4004, Eau Claire, WI 54702-4004

AND

C. KOUVELIOTOU AND T. M. KOSHUT
Universities Space Research Association, NASA/Marshall Space Flight Center, Huntsville, AL 35812
Received 1996 December 18; accepted 1997 June 13

ABSTRACT

It is shown in this study that two different types of spectral emission are generally produced in gamma-ray bursts. A subset of bursts is identified that exhibits a marked lack of fluence above 300 keV, and these bursts are shown to have luminosities about an order of magnitude lower than bursts with significant fluence above 300 keV. The bursts lacking emission above 300 keV exhibit an effectively homogeneous intensity distribution. In addition, it is shown that both types of emission are common in many bursts, demonstrating that a single source object is capable of generating both of them. These results strongly favor a gamma-ray burst source object that produces two different types of emission with varying degrees of superposition. The impact of this behavior is strong enough that it affects the properties of the burst intensity distribution, as well as the burst spectral characteristics.

Subject headings: gamma rays: bursts — radiation mechanisms: nonthermal

1. INTRODUCTION

Several investigators have used the spectral properties of gamma-ray bursts (GRBs) observed by BATSE (Fishman et al. 1989) to identify subclasses that exhibit distinct intensity distributions (Belli 1995; Kouveliotou et al. 1996). Cuts applied to distributions of hardness ratios of the BATSE 100–300 keV fluence over the 50–100 keV fluence (Kouveliotou et al. 1996) have been used that isolate burst subsets whose intensity distributions are nearly homogeneous. In some analyses, information about the burst durations has been used to determine how the hardness ratio cut is applied (Belli 1995). These analyses all show that subsets of bursts that are softer in the 50–300 keV range, that is, bursts with smaller hardness ratios as they are defined above have $\langle V/V_{\max}\rangle$values close to 0.5, the value expected for a homogeneous distribution.

In earlier studies of the gamma-ray burst population's spectral continuum properties, using the BATSE 1B data set (Pendleton et al. 1994), a subclass of events was identified based on a marked lack of emission above 300 keV. At the time the set was found to be distributed isotopically on the sky, but there were not enough events to study the intensity distribution accurately. The presence of this subset in the earlier study of a smaller data set, however, raised the possibility that the significance of the spectral difference between the bursts that exhibit a nearly homogeneous spatial distribution and the rest of the burst population might be strongest at higher energies ($E > 300$ KeV) and that a test for separating the bursts into two distinct classes should be applied to the burst spectra in a higher energy range than 50–300 keV.

In the work presented here, a high-energy spectral cut is used to separate bursts into two types: those with high-energy emission, referred to hereafter as high-energy bursts, or HE bursts, and those without high-energy emission, referred to as no-high-energy bursts, or NHE bursts. The set of NHE bursts appears isotropic with $\langle\cos\ \theta\rangle = -0.026 \pm 0.037$ and $\langle\sin^2 b\rangle = 0.332 \pm 0.018$. The current data set is large enough to examine the intensity distributions and spectral properties of these two types of bursts. However, a larger data set and more extensive tests will be required to determine whether the HE and NHE bursts represent two distinct forms of emission or the extremes of an intrinsic hardness-intensity correlation.

The analysis in each of the following sections is summarized briefly below. This summary serves to define the flow of the entire analysis and present key concept definitions in a concise manner. In § 2, the spectral analysis technique that has been applied to 882 bursts is developed, and evidence is presented for the existence of the HE and NHE burst populations. The high-energy spectral index cut used to separate the two types of bursts is also defined here. In § 3, the intensity distributions of the HE and NHE burst subsets are examined, and measures of their shape are defined and used to quantify the intensity range where the distributions are consistent with homogeneity. It is found that the NHE distribution is consistent with homogeneity to significantly lower peak flux intensity levels than the HE

distribution. Some simple assumptions about the burst population geometry are invoked, and under these assumptions estimates of the luminosity ratios of HE to NHE peak fluxes are calculated.

In § 4, tests are developed to assess the impact of selection effects on the observed homogeneity in the NHE burst intensity distribution. In § 5, evidence is presented showing that there are HE bursts that contain within them identifiable emission peaks that lack high-energy flux. These peaks are referred to as no-high-energy peaks, or NHE peaks. Emission peaks with significant high energy flux are referred to as high-energy peaks, or HE peaks. At this point we have four definitions: two burst types, and two peak types. NHE bursts, containing no high-energy emission during the entire event, are composed of one or more NHE peaks. HE bursts, which do contain high-energy flux, contain at least one HE peak and may contain a number of other HE or NHE peaks. It is only the HE bursts that are found to contain both types of peaks. The peak identification algorithm is described in Appendix A.

In § 6, the results of spectral analysis on the peaks within the bursts is presented. The peaks are divided into three groups: HE peaks from HE bursts, NHE peaks from HE bursts, and NHE peaks from NHE bursts. The spectral properties of these emission peak populations are compared. It is found that the NHE peaks from the two different types of bursts are quite similar. In § 7, the intensity distribution of the NHE peaks within HE bursts is calculated, and its shape evaluated for comparison with the intensity distribution of the NHE bursts themselves. A study of selection effects on this procedure is presented in Appendix B. In the discussion, the results of §§ 2–7 are reviewed, and the reasons are given why it is likely that the NHE and HE bursts are produced by the same source object. The burst luminosity function is also discussed.

2. THE BROAD ENERGY BAND SPECTRAL ANALYSIS TECHNIQUE AND THE HIGH-ENERGY SPECTRAL INDEX CUT

The four-channel spectral analysis technique described below is valuable for population studies because it can be used to calculate spectral information, albeit with poor energy resolution, for even the weakest bursts observed by BATSE. Therefore, it is particularly useful when evaluating the existence of burst subpopulations based on spectral characteristics. For this analysis, the model-independent spectral analysis is applied to a set of 882 gamma-ray bursts using the BATSE Large Area Detector (LAD) discriminator data. These data are binned in four broad energy channels: 25–50 keV, 50–100 keV, 100–300 keV, and $E > 300$ keV. The data are summed over the burst triggered LADs with 64 ms time resolution. The source counts are isolated for each channel using polynomial fits to background intervals before and after the burst.

A direct matrix inversion technique that has been applied successfully to observations of SN1987A (Pendleton et al. 1995a) is used here to convert the LAD discriminator spectra from counts to photons. For direct inversion, the initial detector response matrix (DRM) (Pendleton et al. 1995b), dimensioned 70×4, must be cast as a 4×4 matrix. Since the bin widths are so wide, some approximation to the spectral shape across each bin is applied. A spectral index of -0.5 is applied across the first three bins and of -1.5 over the highest bin range of 300–6500 keV. The fourth discriminator channel is actually unbounded on the high end. However, the energy range cited above was found to be effective for bursts and for the Crab Nebula flux measured using four channel earth occultation data (Pendleton et al. 1994). The 70 incident energy vectors of the DRM are separated into four contiguous sets appropriate for four broad incident photon bins. These vectors are then weighted using the power-law spectral form with the indices cited above and then summed across the energy range of each broad bin to produce square 4×4 DRMs for direct inversion. This procedure has the effect of producing a DRM that assumes a particular spectral form across each of the four broad energy bins. Experience with gamma-ray data from the Crab nebula and SN 1987A indicates that if the spectral indices are within about ± 1 of the actual underlying continuum spectral index, then the direct matrix inversion technique is accurate to $\sim 15\%$. We start with our set of initial GRB spectral indices listed above using them only to construct the DRM and proceed with a first direct spectral inversion of the four-channel data.

The DRMs from the separate detectors are summed for use with the summed peak flux data. Then the DRM is inverted and used to produce the photon spectrum using this relation:

$$\mathrm{DRM}^{-1} \times \mathrm{counts} = \mathrm{photons}\ . \qquad (1)$$

At this point, the four-channel photon spectrum is expressed as log (photons cm^{-2} KeV^{-1}) versus log (energy) with each point at the logarithmic bin center. These data, expressed logarithmically, are then linearly interpolated to 12 points across the response matrix energy range. A quadratic is fit to these data in order to estimate the continuum spectral form across each bin. In this procedure, we are not trying to get the most accurate fit to the spectrum with this quadratic fit; we are simply trying to get a somewhat better approximation to the burst's spectral form than the initial indices used to construct the first matrix for inversion. The four-channel photon data and the polynomial fit to them are shown in Figure 1 for the total emission from 3B 930506.

The quadratic polynomial is then used to build a 4×4 matrix from the original 70×4 matrix a second time by weighting the input elements across each broad bin by the quadratic form across that bin. This is the only place where this quadratic fit is used. The spectral inversion is performed again using this new matrix applied to the same counts data, and the final photon fluxes are obtained. It is found that the spectra are stable at this point (i.e., further iterations of this procedure do not change the results significantly). This spectral analysis procedure is also described in detail elsewhere (Pendleton et al. 1994; Pendleton et al. 1996; Fishman et al. 1994). Each four-channel, 64 ms photon spectrum within the burst is calculated in this way, producing four-channel photon flux histories, some of which are shown below.

The bursts exhibit a variety flux histories with a broad range of durations and complexity. However, most bursts exhibit significant fluence above 300 keV. Figures 2*a*–2*c* show the flux histories of three bright bursts in the four LAD discriminator energy channels. The fluxes are shown in photons cm^{-2} s^{-1} in each bin with 64 ms resolution. The bursts in Figures 2*a*–2*c*, although they show significant spectral evolution, all have significant fluence above 300

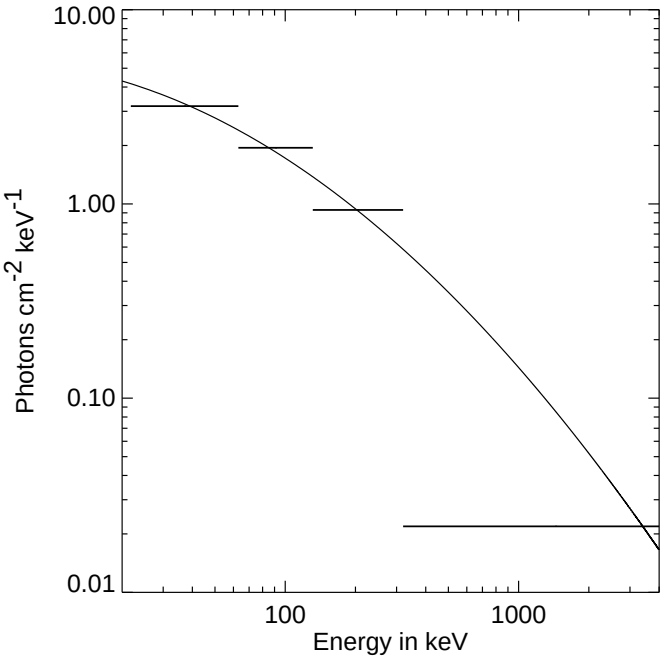

FIG. 1.—Plot of four-channel photon fluence data for burst 3B 930506. The direct inversion results are shown as the data points. A quadratic fit to the data, used in the construction of the DRM for direct inversion, is also shown.

keV for most of their duration. These are the high-energy, or HE, bursts.

However, there are also bursts that appear to have no visible emission above 300 keV. Figures 3*a*–3*c* show examples of this kind of burst, the no-high-energy, or NHE, bursts. The rates above 300 keV shown in the figures for these bursts are dominated by the statistical fluctuations about a background-subtracted source flux value of zero. In some of these bursts there may be a small amount of flux above 300 keV near the beginning of the burst; however, the bulk of the burst emission occurs without high-energy fluence. In the 100–300 keV range these NHE bursts show strong emission, with fluences present at greater than the 60 σ level. For example, burst 3B 920622B shown in Figure 3*a* has a total 100–300 keV fluence significance of 61 σ. The channel 4 fluence measurement is $-0.5\ \sigma$. This represents a very significant spectral cutoff. If this burst actually had a fluence high-energy hardness ratio as large as the HE bursts in Figures 2*a*–2*c*, then the channel 4 fluence would have been significantly larger, as is shown in Table 1. This burst, and the other two bursts shown in Figures 3*b* and 3*c*, are decisively softer at high energies than the HE bursts.

TABLE 1

HARDNESS ADJUSTMENT TABLE

Comparison Burst	σ Increase[a]
3B 930506	25
3B 920517	8
3B 930110	16

[a] σ Increase is the amount by which the fluence in channel 4 of 3B 920622 must be raised to match the channel 4 fluence of the comparison burst.

These data show that there are at least a few NHE bursts, but it is useful to present evidence for the existence of a subpopulation (i.e., a fairly significant number) of them. Finding this evidence requires more than simply examining the burst population and selecting bursts with small hardness ratios. The hardness ratio distribution is broader when the bursts in it have larger error bars on their fluence measurements. In this case the observed distribution can be much broader than the true, or parent, distribution (i.e., much broader than what we would observe with an instrument possessing infinite sensitivity). Therefore, some of the bursts at the extremum of the observed hardness ratio distribution, for instance, in the NHE region, may be weaker events that ended up there because of statistical fluctuations, but would actually have been classified as HE bursts by a considerably more sensitive instrument. The size of the fluence errors are strongly correlated with burst intensity and duration. We will examine the intensity dependence in subsequent sections and concentrate on the duration dependence below.

In Figure 4 we plot histograms of the hardness ratios of the photon fluences in DISCLA channel 4 ($E > 300$ kev) over DISCLA channel 3 (100–300 kev) separated into three duration intervals: $T_{90} > 10$ s, $10\ \text{s} > T_{90} > 1.024$ s, and $1.024\ \text{s} > T_{90} > 0.384$ s. The T_{90} values, or durations (Koshut et al. 1996), are the same as those in the 3B catalog (Meegan et al. 1996). There are three histograms in each interval: one of actual data, and two from simulations. The thick-lined histogram with the broader bins is observed data for bursts where the 256 ms peak flux of the bursts was greater than 0.65 photons $\text{cm}^{-2}\ \text{s}^{-1}$.

We have separated the bursts by duration because we know that the longer bursts have smaller errors on their total emission hardness ratios than the shorter bursts. We want to see if the NHE bursts (i.e., bursts that lack high-energy fluence) are predominantly the shorter bursts or not. The top panel in Figure 4 shows that there are a significant number of bursts with hardness ratios consistent with zero, even for the longer bursts. There is even a slight suggestion of a clustering of bursts around zero, although there are not enough events to confirm it. We can, however, test to see whether the statistical errors are small enough to resolve such a clustering using a Monte Carlo simulation.

To do this we take as a parent or true distribution the actual channel 3 and 4 photon fluences used to produce the histogram of observed hardness ratios in the top panel of Figure 4. For each measurement we resample the channel 3 and 4 values repeatedly from a normal distribution with an average equal to the actual data value and a standard deviation equal to the error on the measured value. This produces a very large set of hardness ratio values, centered about the data values, but distributed with their characteristic errors. In this way we can produce a histogram that reveals the shape of the underlying hardness ratio distribution as well as it can be resolved using data characterized by the observation errors, under the assumption that the observed data is a reasonably representative sample of the true hardness ratio distribution. These histograms are represented by the darker of the finely binned histograms in Figure 4. For the bursts in the top panel, the simulations indicate that a clustering of bursts around a hardness ratio of zero is resolvable with data of this accuracy.

For the shorter burst sets, shown in the lower two panels, the NHE bursts are merged smoothly into the rest of the

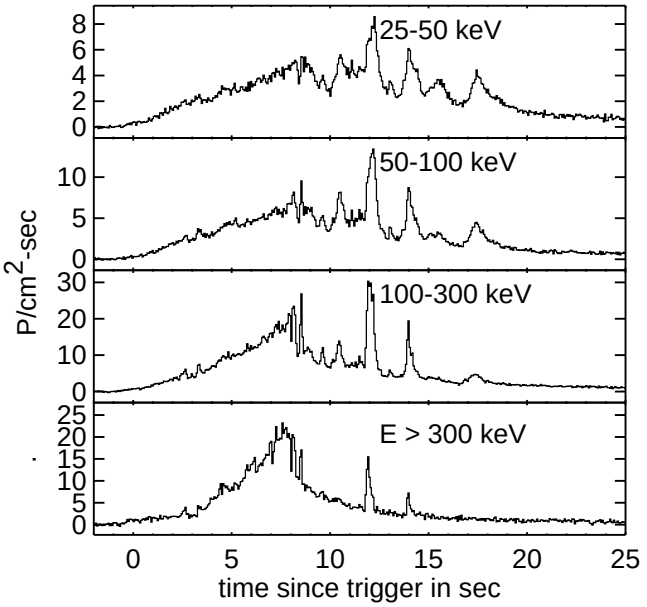

FIG. 2*a*

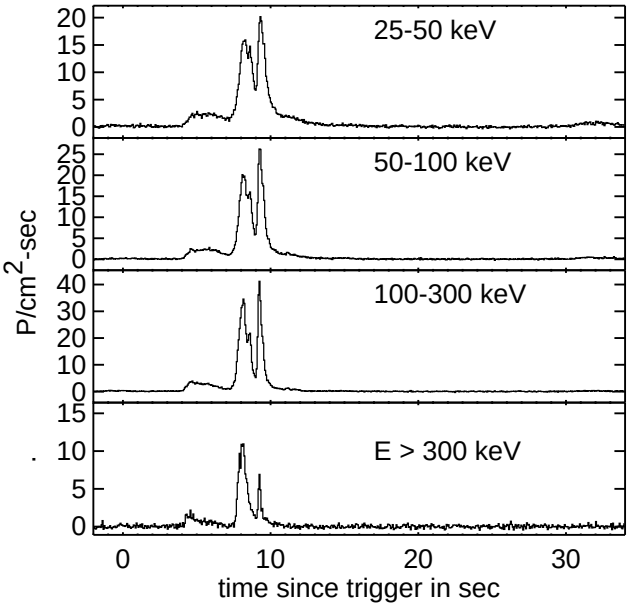

FIG. 2*b*

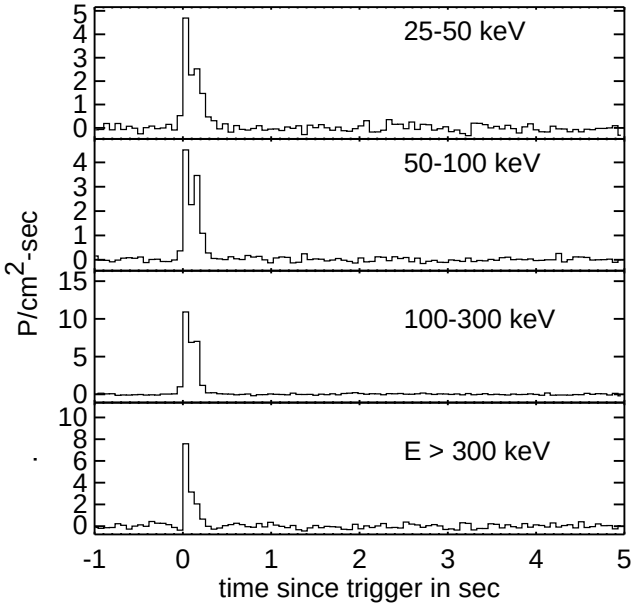

FIG. 2*c*

FIG. 2.—Flux histories for HE bursts shown here in physical units of photons cm^{-2} s^{-1} with 64 ms resolution. The four BATSE LAD discriminator channels are shown separately.

burst population, indicating that further tests are required to determine what fraction of these bursts are likely to be true NHE bursts. In order to study this more closely, we have run simulations where we assume all the bursts have hardness ratios between 0.1 and 0.55 but have errors characteristic of the entire data set. The procedure follows that of the first simulation with a few differences. We select the channel 3 photon fluence and the channel 3 and 4 errors as before. The channel 4 photon fluence is calculated by drawing a random sample from the hardness ratio histogram of the observed data between the values of 0.1 and 0.55 and multiplying by the channel 3 photon fluence. The actual simulation sample is then calculated as before, using the normal distribution sampling technique described above.

This procedure produces a hardness ratio data set that represents what would be observed if the parent hardness ratio distribution were actually limited to between 0.1 and 0.55, with a shape like that seen in the data, and an instrument with BATSE's sensitivity was used. We can use this to test the hypothesis that all the bursts actually have high-energy flux and determine what fraction of them end up being measured as NHE bursts because of statistical fluctuations. The results are shown as the lighter finely binned histograms in Figure 4. They show that the shorter NHE bursts are significantly contaminated by statistical fluctua-

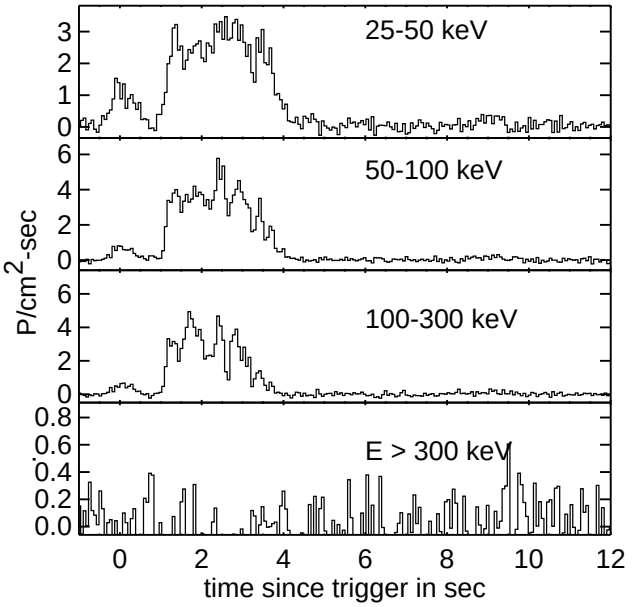

FIG. 3*a*

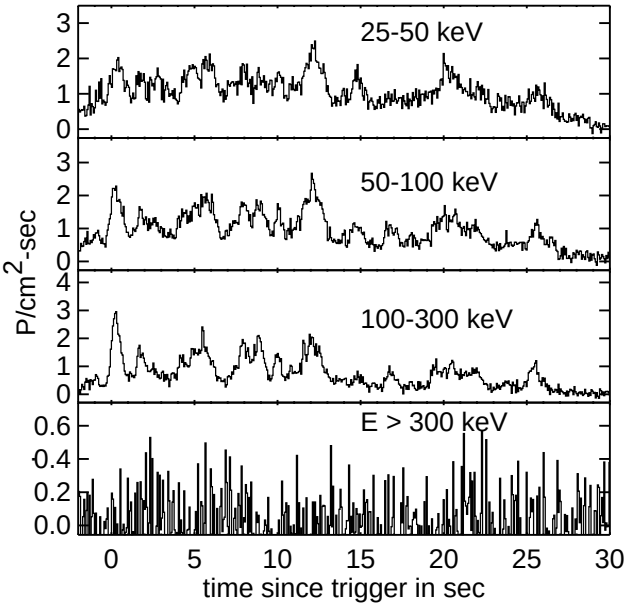

FIG. 3*b*

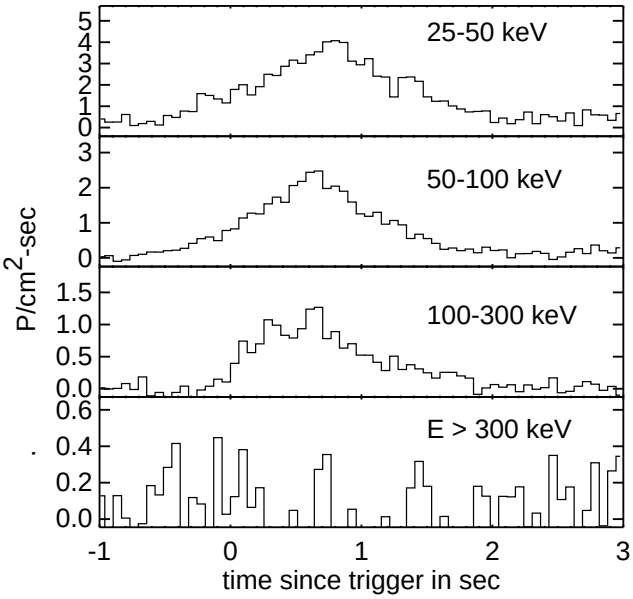

FIG. 3*c*

FIG. 3.—Flux histories for NHE bursts shown here in physical units of photons cm^{-2} s^{-1} with 64 ms resolution. The four BATSE LAD discriminator channels are shown separately.

tions from the HE burst set, But the longer NHE bursts are largely unaffected. These results will be discussed more quantitatively in § 4. However, at this point the analysis shows that there is evidence for both individual bright NHE bursts, and for a population of NHE bursts, clearly distinguished for the longer bursts.

The hardness ratio in physical units still incorporates the bin width dependence of the particular energy bins used for the data in the ratio. It is possible to define an effective power-law spectral index that provides a first-order representation of the spectral behavior in the energy range spanned by the bins used in the hardness ratio. This representation of the spectrum will not be identical to that obtained with a forward-folding model-fitting technique applied to higher energy resolution data, since it will reveal only the low-energy-resolution, first-order spectral characteristics of the bursts. However, the results will be useful for comparison studies of the similarities and differences between burst subsets since all the values are calculated in the same way. The technique is quite robust, so it can be applied effectively even to weak bursts, and therefore is particularly suited to large population studies. Furthermore, the technique is effectively model-independent, so the results will not be biased by a potentially inappropriate choice for the spectral form that might be difficult to detect for weak bursts. We have calculated these spectral indices in

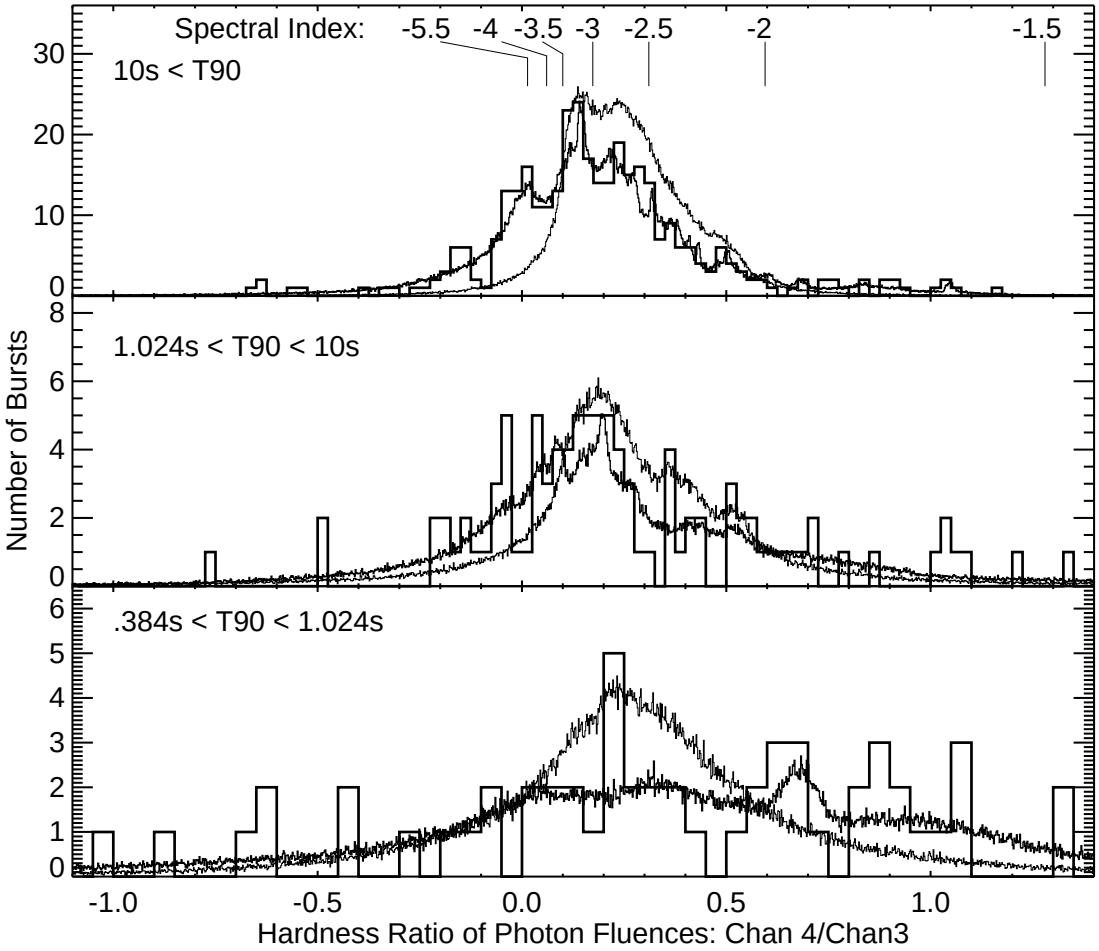

FIG. 4.—Histograms of total emission hardness ratio distributions in the $E > 100$ keV range plotted vs. the 64 ms peak flux for the burst population. The bursts are separated by duration with the longest bursts in the top panel and the shortest bursts in the bottom panel. The thick-lined broadly binned histogram is the actual data, and the finely binned histograms are simulation results.

three energy ranges: 25–100 keV, 50–300 keV, and $E > 100$ keV. The errors on the spectral indices are calculated in hardness ratio units and then converted to spectral index.

Equation (2) uses the $E > 100$ keV energy range as an example of the effective spectral index calculation:

$$\frac{\int_{300}^{6500} E^{\alpha 43} dE}{\int_{100}^{300} E^{\alpha 43} dE} = \frac{P_4}{P_3}. \quad (2)$$

Here P_4 is the fluence in photons cm^{-2} in the $E > 300$ keV bin, P_3 is the fluence in the 100–300 keV bin, and α_{43} is the power law index used in the integrand. There is a monotonic mapping of power-law spectral index to this hardness ratio. In the top panel of Figure 4, the mapping of hardness ratio to spectral index is indicated for the $E > 100$ keV energy range. The thin vertical lines connect the effective spectral index values to the appropriate hardness ratio values. The energy edges of the data bins for each detector differed slightly from the ideal values shown here because of variation in calibration between detectors. For the analysis of each burst the bin edges of the brightest detector were used. The spectral index tends toward negative infinity as the hardness ratio approaches zero, so a lower limit of -6 is used for any hardness ratio less than or equal to that associated with a spectral index of -6.

This technique, although it has limits particularly in the area of energy resolution, is very robust and well suited to burst population studies that include many weak bursts. The value of α_{43} should not be considered representative of what the burst spectrum is like at energies significantly higher than 300 keV; it is a first-order representation of what the burst spectrum is like around 300 keV. More detailed analyses may reveal a more sophisticated method for separating HE and NHE bursts. However, the current definition is adequate to identify the features in the burst data of interest here.

In the subsequent analysis, NHE bursts are defined as those bursts where $\alpha_{43} < -5.5$ for the burst fluence interval. This selection is meant to reduce the contamination by weak HE bursts of the NHE burst subset for subsequent studies of the burst's intensity distributions. The spectral cut defined in physical units in the high-energy range has some advantages over spectral cuts defined in counts, or in the peak flux energy range. The data expressed in photons instead of counts have been corrected for detector response, and so potential systematic effects have been removed. Also, as will be seen in § 4, the effect of intrinsic correlation between spectral index and intensity in the 50–300 keV range can be directly assessed. However, decisive evidence that favors this spectral cut over those proposed by others

will require significantly larger data sets, since we will have to examine the intensity distributions of those parts of the selected subsets that do not overlap, and we do not have enough bursts to do this effectively at present.

3. IDENTIFICATION OF DISTINCT INTENSITY DISTRIBUTIONS BASED ON A HIGH-ENERGY SPECTRAL INDEX CUT

In this section we will define measures of the shape of the intensity distribution and apply them to the HE and NHE burst sets on the three BATSE trigger timescales. In the following section we will take a skeptical approach to the nature of the homogeneous NHE set to explore how the effects of the intensity dependence of the index errors and other possible selection effects might influence the shape of its intensity distribution.

Figure 5 displays the integral intensity distributions of the HE bursts (*thick histograms*) and NHE bursts (*thin histograms*) on the three BATSE trigger timescales. The dashed, slanted lines tangent to each distribution represent the $-\frac{3}{2}$ power-law shape of a homogeneous intensity distribution. It is qualitatively clear that the NHE distributions appear to be homogeneous to lower intensities than the HE bursts, although they deviate from homogeneity near threshold on the longer timescales.

The intensity distribution of the NHE bursts on the 64 ms timescale appears to be homogeneous right down to the instrument threshold, whereas on the 256 ms and 1024 ms timescale, the distributions deviate from homogeneity right around threshold. To determine whether or not these deviations of the NHE distributions from homogeneity are purely instrumental or not, we can apply the conventional $\langle V/V_{\max}\rangle$ test (Schmidt et al. 1988) to these bursts. For the 154 NHE bursts with calculated $C/C_{\lim}$ values, we chose the maximum $C/C_{\lim}$ value from the three trigger timescales for each burst. The resulting $\langle V/V_{\max}\rangle$ value for the NHE bursts is 0.43 ± 0.023. This is 3 σ away from the value of 0.5 expected for homogeneity, indicating that the NHE bursts deviate from homogeneity, within the intensity range covered by BATSE.

In this analysis, we wish to explore the nature of the deviation of the NHE burst's intensity distribution from homogeneity more precisely. We use an expression analogous to $\langle V/V_{\max}\rangle$, except that the peak fluxes are expressed in physical units: photons cm^{-2} s^{-1}. The expression is similar to one developed by Horack & Emslie (1994):

$$V_p/V_{\rm plim} = (P/P_{\lim})^{-3/2} . \quad (3)$$

In this case we add the constraint that the intensity distribution should be measured only down to flux levels, $P_{\lim}$, where the instrument sensitivity starts to significantly affect the shape of the observed intensity distribution, and not below that intensity level. For this analysis, the $P_{\lim}$ values have been chosen so that the exposure for the weakest bursts is at least 70% of the exposure for the brightest bursts. This places $P_{\lim}$ at a level where the current sky map corrections start to take effect and where the deviation of the sky-map–corrected cumulative distributions from the measured distributions is not significant. In fact, since the current correction neglects atmospheric scattering, the exposure is, in reality, better than we are quoting here. These arguments are presented in detail elsewhere (Pendleton et al. 1996). If the intensity distribution above $P_{\lim}$ is homogeneous, then $\langle V_p/V_{\rm plim}\rangle = 0.5$.

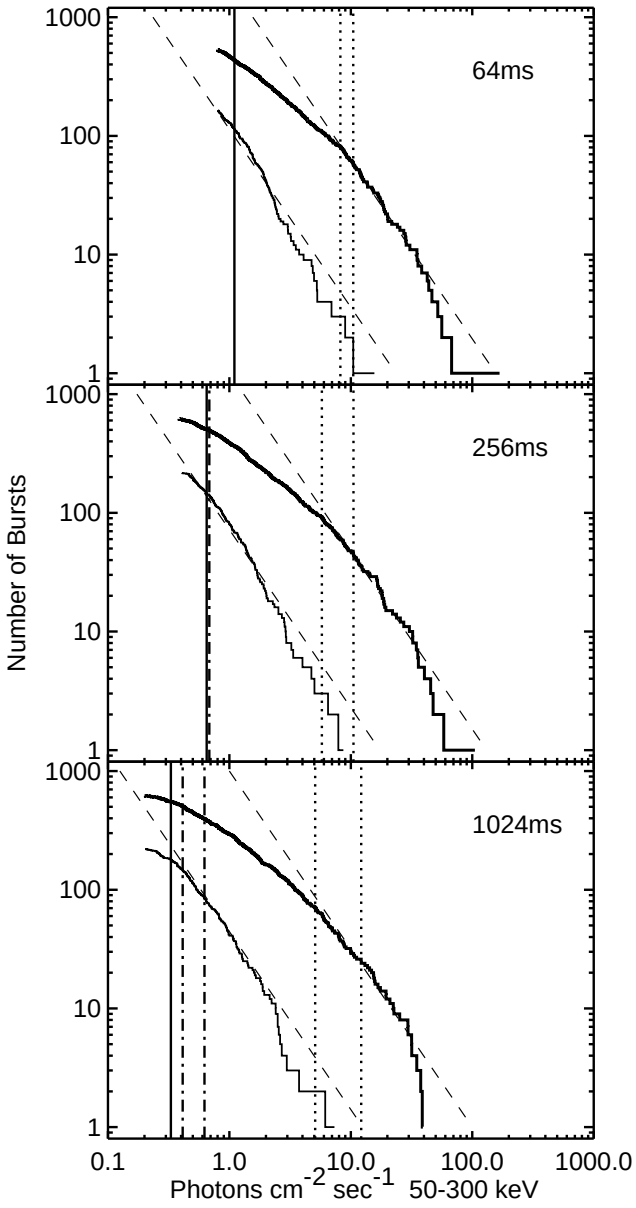

FIG. 5.—Intensity distributions on the three trigger timescales for the HE bursts (*thick-lined histogram*) and the NHE bursts (*thin-lined histogram*). The solid vertical lines at the low intensity end of the distributions show where instrument threshold effects become important. The dotted vertical lines show the intensity range where the HE distributions break from homogeneity. The dashed vertical lines show the intensity range where the NHE distributions break from homogeneity.

Table 2 summarizes the results of the analysis of the data presented in Figure 5. The absolute instrument thresholds on each timescale are shown in row (1). Rows (2) and (3) show the numbers of bursts of each type above this threshold. The intensity distributions in Figure 5 are plotted down to the thresholds in row (1). In row (4) the ratios of the number of NHE bursts above threshold to the total number of bursts are shown in percent. About one-quarter of the observed bursts are in the NHE set as can be seen from these ratios. Rows (6) and (7) show the numbers of bursts above the thresholds, $P_{\lim}$, shown in row (5) and depicted as solid vertical lines in Figure 5. These bursts occur in the intensity range where BATSE can reliably measure the

TABLE 2

INTENSITY DISTRIBUTION PARAMETERS FOR HE AND NHE BURSTS

Quantity	64 ms	256 ms	1024 ms
1. Threshold	0.8	0.4	0.2
2. No. NHE_{thresh}	166	218	222
3. No. HE_{thresh}	532	615	620
4. NHE/TOT_{thresh} (%)...	23.8	26.2	26.4
5. Exposure cutoff.....	1.2	0.65	0.33
6. No. NHE_{cut}	103	145	179
7. No. HE_{cut}	406	507	552
8. NHE/TOT_{cut} (%)	20.2	22.2	24.5
9. $\langle V/V_{pcut}\rangle$ (HE).....	0.34 ± 0.014	0.31 ± 0.012	0.27 ± 0.011
10. $\langle V/V_{pcut}\rangle$ (NHE)	0.54 ± 0.026	0.48 ± 0.022	0.43 ± 0.02
11. DR_{low}	>1.2	>1.5	3.5–5.9
12. DR_{high}	>1.7	>3.2	1.2–2.1
13. LR_{low}.....	>8.3	$>10.$	8.8–11.7
14. LR_{high}	$>10.$	>15.2	16.6–22.4
15. LR_{bright}	8.3	9.3	9.1

NOTE.—Threshold = peak flux threshold. No. NHE_{thresh} = number of NHE bursts above threshold. No. NHE_{cut} = number of NHE bursts above the cutoff. DR_{low} = ratio of the number of NHE to HE bursts within the homogeneous volume for HE volume lower edge. DR_{High} = ratio of the number of NHE to HE bursts within the homogeneous volume for HE volume higher edge. LR_{low} = luminosity ratio of HE to NHE bursts within the homogeneous volume for HE volume lower edge. LR_{High} = luminosity ratio of HE to NHE bursts within the homogeneous volume for HE volume higher edge. LR_{bright} = luminosity ratio of the brightest 20 HE to the brightest 20 NHE bursts.

shape of the bursts' physical intensity distribution. Row (8) shows the same ratios as those in row (4) for bursts above the thresholds in row (5), demonstrating that NHE bursts comprise one-quarter to one-fifth of the total population observed in this intensity range. The row (5) $P_{\rm lim}$ values are used as the thresholds for the $\langle V_p/V_{\rm plim}\rangle$ values given in rows (9) and (10). The $\langle V_p/V_{\rm plim}\rangle$ values in row (9) show that the HE burst intensity distributions deviate significantly from isotropy, as has been shown in many earlier analyses (Fishman et al. 1994; Meegan et al. 1996; Pendleton et al. 1996). Row (10) shows the values for the NHE bursts, and only the 1024 ms distribution deviates significantly from homogeneity.

At this point it is useful to develop a method for defining the range over which the observed intensity distributions break from homogeneity. Given the relatively low statistics for the burst sets in the homogenous intensity range, this definition will be somewhat coarse, but adequate for out present purposes. We calculate $\langle V_p/V_{\rm plim}\rangle$ as a function of intensity for each distribution. We pick as the upper edge of our homogeneity break range the lowest intensity where $\langle V_p/V_{\rm plim}\rangle \geq 0.5$. The lower bound is the lowest intensity where $\langle V_p/V_{\rm plim}\rangle + 1\ \sigma \geq 0.5$. For the HE burst distributions, these ranges are shown by the dotted vertical lines in Figure 5. For the NHE distributions, the ranges are bounded by vertical dot-dashed lines. On the 64 ms timescale the NHE break never even starts, while on the 256 ms timescale only the upper edge of the NHE break range is visible. It is completely specified only on the 1024 ms timescale.

All subsets of bursts identified so far show homogeneity for at least their brightest bursts. In most cosmological or extended galactic halo models, the nearby sources are distributed homogeneously while the more distant sources appear to be less numerous. If we make one of the simplest assumptions about the spatial distribution for bursts, and also assume that the luminosity distributions for the two types of GRBs are not overly large, then we can make some first order estimates of the relative luminosities and source densities of the HE and NHE bursts. The assumption about the burst spatial distribution we will use for the following analysis is that the homogeneous parts of the intensity distributions represent bursts that occupy the same region of space; that is, the distance at which deviation from homogeneity becomes apparent is the same for all the burst sets. This would be the case if both types of burst are produced by the same type of source objects.

Since we have calculated the homogeneity break ranges as described above, we can then select all bursts above the break intensities and calculate the average of the homogeneous burst intensities. Using the assumptions stated above, the ratios of these averages gives the ratios of the average peak luminosities for the two types of bursts. In addition, the number of each kind of burst within the homogeneous part of the set gives an estimate of the relative source density per unit volume.

The density ratios of the NHE to HE bursts are shown in rows (11) and (12) of Table 2. The density ratios (DR_{low}), based on the lower edge of the HE burst intensity break range, are given in row (11). Only lower limits can be calculated for the 64 ms and 256 ms timescales since the NHE break ranges cannot be completely specified there. The DR_{low} range given in the 1024 ms column is calculated from the upper and lower edges of the 1024 ms NHE break range. The density ratios based on the upper edge of the HE burst intensity break range are given in row (12). The density ratios are all greater than one, which suggests that we observe more NHE bursts per unit volume than HE bursts. This could mean that the sources produce purely NHE emission more often than they produce HE emission, or that the HE emission is more tightly beamed than the NHE emission.

The luminosity ratios shown in rows (13) and (14) are calculated by finding the average intensity of the homogeneous part of each set, as identified by the homogeneity break range boundaries described above, and then calculating the appropriate HE to NHE ratios. The sets used to calculate the ratios in rows (13) and (14) of Table 2 are the same as those employed in the density ratio calculations summarized in rows (11) and (12). These calculations indicate that the HE bursts are about an order of magnitude brighter than the NHE bursts, although there is obviously a broad range of possibilities.

We can also take the ratio of the peak fluxes of the 20 brightest bursts of each type and calculate the luminosity ratios from them. These values are given in row (15) of Table 2. These numbers are at the lower end of the ranges shown in rows (13) and (14). The density ratio values indicate that this could be due to the homogeneous NHE data set being larger than the homogeneous HE data set. The larger sample size would bias the brighter NHE bursts to larger values relative to the brighter HE bursts, an effect that can be verified with simple Monte Carlo calculations. Hence, if the density ratios for the two types of bursts are different, as these analyses suggest, then the luminosity ratios in rows (13) and (14) will be more accurate, although less precise.

It is important to remember that these estimates are still crude, and a larger data set will be necessary to improve their precision substantially. In addition to increasing the size of the data set, more precise estimates of the intensity

distribution break points will be possible if particular models of the spatial and luminosity distributions of the burst sources are assumed and fit to the observed data. This kind of detailed modeling will be reserved for future work.

4. EXPLORATION OF POTENTIAL STATISTICAL AND SYSTEMATIC EFFECTS ON THE INTENSITY DISTRIBUTION OF NHE BURSTS

In the previous section we established that the break in the NHE bursts' intensity distribution from homogeneity occurs at significantly lower peak flux levels than for the HE burst distribution. We also established, using the analysis presented in Figure 4, that some number of true NHE bursts exist, although the set of observed NHE bursts with shorter durations is heavily contaminated by HE bursts due to the poorer statistics of the measurements. We must now consider how this selection effect impacts the shape of the NHE burst intensity distribution.

How much of the observed homogeneity in the NHE burst distribution is due to contamination by weaker HE bursts? As we stated above, the population of longer NHE bursts has much less weak HE burst contamination than the shorter NHE set. Therefore, if the NHE homogeneity is predominantly due to contamination of the observations by weak HE bursts, then we should see a marked difference between the intensity distributions of the short NHE bursts and the long NHE bursts.

In Figure 6 we show a scatter plot of the high-energy effective spectral index of the entire burst emission versus the T_{90} duration for bursts with 256 ms peak flux values greater than 0.65 photons cm^{-2} s^{-1}. The error bars are omitted from all but a few of the shortest bursts for clarity. They are included on those bursts to emphasize the uncertainty on their spectral index measurements that appear to be quite hard. The NHE bursts assigned a spectral index value of -6 are shown in the far left of the plot. This figure confirms the duration bimodality and the hardening of burst fluence with duration reported earlier (Kouveliotou et al. 1993), except that here we are examining the spectrum in a higher energy range. It is also useful in illustrating the procedures we use to probe for selection effects in the NHE intensity distribution. The bursts are separated into four duration intervals and four spectral index ranges resulting in 16 subsets of bursts. The subset boundaries are marked by the solid horizontal and vertical lines in Figure 6. We have calculated the $\langle V_p/V_{\rm plim}\rangle$ values for each of the subsets and these are shown in Table 3. Next to each $\langle V_p/V_{\rm plim}\rangle$ value in this table is its error and the number of bursts in the sample. The NHE bursts all have $\langle V_p/V_{\rm plim}\rangle$ values consistent with 0.5, even those with durations longer than 10 s.

If we compare the simulation results shown in Figure 4, where the darker finely binned histogram assumes the existence of NHE bursts and the lighter finely binned histogram assumes that all bursts with spectral indices less than -3.5 are the result of statistical fluctuation, we can get an estimate of the percentage of weak HE burst contamination in each duration interval. We calculate the ratio of the total of the lighter histogram summed up to -5.5 and divide by the total of the darker histogram summed over the same interval to obtain this percentage. In the 0.384 s $<$ 1.024 s interval, the contamination percentage is 80%. This is a high level, and we would expect the shape of the intensity distribution to be dominated by this effect. In the 1.024 s $<$ T_{90} $<$ 10 s interval, the ratio is 51%. This is still a high level, so the true underlying NHE intensity distribution shape could very well be masked. In the T_{90} $>$ 10 s interval, the contamination percentage is 20%. Here we would expect the $\langle V_p/V_{\rm plim}\rangle$ value to deviate significantly from 0.5 if, in fact, the NHE distribution itself deviated significantly from homogeneity. It is this data subset that provides the most convincing evidence that the NHE bursts have a more homogeneous intensity distribution than the HE bursts.

We can check the sensitivity of this test by examining the distributions at the hard extreme of the spectral index distribution. We can calculate the statistical contamination using the same method as for the NHE bursts, except here

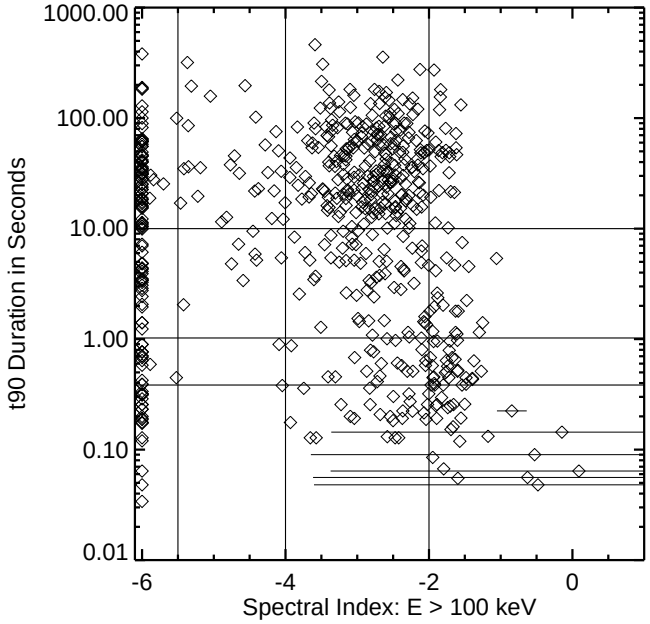

FIG. 6.—Scatter plot of effective spectral index in the $E > 100$ keV range vs. duration for bursts with peak fluxes greater than 0.65 photons cm^{-2} s^{-1} on the 256 ms timescale. The vertical and horizontal lines divide the bursts into 16 subsets. The shapes of the intensity distributions of these subsets are characterized by the data presented in Table 3 and are discussed in § 4.

TABLE 3

VALUES OF $\langle V_p/V_{\rm plim}\rangle$, ERRORS, AND NUMBER OF BURSTS FOR BURST POPULATION SUBSETS

BURST PROPERTY	INDEX < -5.5		$-5.5 <$ INDEX < -4		$-4 <$ INDEX < -2		$-2 <$ INDEX	
	Value and Error	N	Value and Error	N	Value and Error	N	Value and Error	N
$T_{90} > 10$ s	0.47 ± 0.031	69	0.36 ± 0.039	27	0.29 ± 0.018	233	0.33 ± 0.066	25
10 s $> T_{90} >$ 1.024 s	0.48 ± 0.056	26	0.24 ± 0.103	8	0.22 ± 0.030	58	0.56 ± 0.069	19
1.024 s $> T_{90} >$ 0.384 s.....	0.51 ± 0.078	15	$0.04 \pm$ N.A.	1	0.31 ± 0.051	19	0.36 ± 0.055	29
0.384 s $> T_{90}$	0.50 ± 0.048	21	$0.37 \pm$ N.A.	1	0.29 ± 0.052	25	0.36 ± 0.064	22

we total the simulation data sets shown in Figure 4 for spectral index values greater than -2, remembering that the lighter histogram data in Figure 4 was generated from a spectral index model cut off at the harder index end as well. For bursts with spectral indices greater than -2 and $T_{90} > 10$ s, the statistical contamination level is 34%. With this level of contamination, the $\langle V_p/V_{\rm plim}\rangle$ is still 2.6 σ less than 0.5. This result indicates that 34% contamination by predominantly weak bursts is not enough to mask the deviation of the burst intensity distribution from a $\langle V_p/V_{\rm plim}\rangle$ of 0.5. In the 1.024 s $< T_{90} <$ 10 s range, the statistical contamination is 64%, and the $\langle V_p/V_{\rm plim}\rangle$ value is consistent with homogeneity. In the 0.384 s $< T_{90} <$ 1.024 s interval, the contamination is 44%, and the $\langle V_p/V_{\rm plim}\rangle$ value once again deviates from homogeneity. These results indicate that the statistical contamination by weak bursts should become dominant somewhere between 45% and 65%. Therefore, the $T_{90} > 10$ s NHE burst subset $\langle V_p/V_{\rm plim}\rangle$ value, having only 20% contamination, indicates that the true NHE burst intensity distribution is significantly more homogeneous than the HE burst intensity distribution.

Unfortunately, these burst subsets are quite small, and about 4 times as much data will be needed to confirm these subset studies and to allow for more detailed modeling of the phenomenon. However, this analysis shows that tests designed to reveal the presence of selection effects in the intensity distributions of bursts selected from the extrema of the burst spectral index distribution yield results that are consistent with an NHE burst subset that is significantly more homogeneous than the rest of the population.

In order to explore the domain of selection effects more fully, we have also performed Monte Carlo simulations that compare the $E > 100$ keV hardness ratio distributions in different intensity ranges. Our initial analyses support the assertion that the NHE bursts are more numerous at lower intensities and that this result is not due to a statistical selection effect. We have also shifted the bright burst hardness ratio distribution to lower values, simulating the $E_{\rm peak}$-intensity correlation previously seen in the data. The results indicate that such a shift does not readily explain the observed hardness ratio distributions either.

We have also explored how potential hardness-intensity correlations affecting the spectrum in the 50–300 keV energy range can influence the intensity distributions, especially when spectral index cuts are used to separate them. Our intensities are defined as the total flux in the 50–300 keV range, and, although the spectral index cut applied here spans the $E > 100$ KeV energy range, the 50–300 keV spectral index distribution of the NHE bursts in the peak flux energy range is on the lower side of the total burst population's 50–300 keV spectral index distribution.

Figure 7 shows the 50–300 keV spectral index distributions for the HE bursts (*thick-lined histogram*) and the NHE bursts (thin-lined histogram). Since the average spectral index for the NHE bursts is lower than that of the HE Bursts, it its worthwhile investigating the impact of potential hardness-intensity correlations in the 50–300 keV energy range on the NHE burst intensity distributions. It is worth noting at this point that the data used to calculate these spectral indices were expressed in photons cm^{-2} bin^{-1} for the 50–100 and 100–300 keV bins, and they were generally within 50% of each other for typical burst spectral index values. The differences in intensity we are probing here are close to an order of magnitude as discussed above,

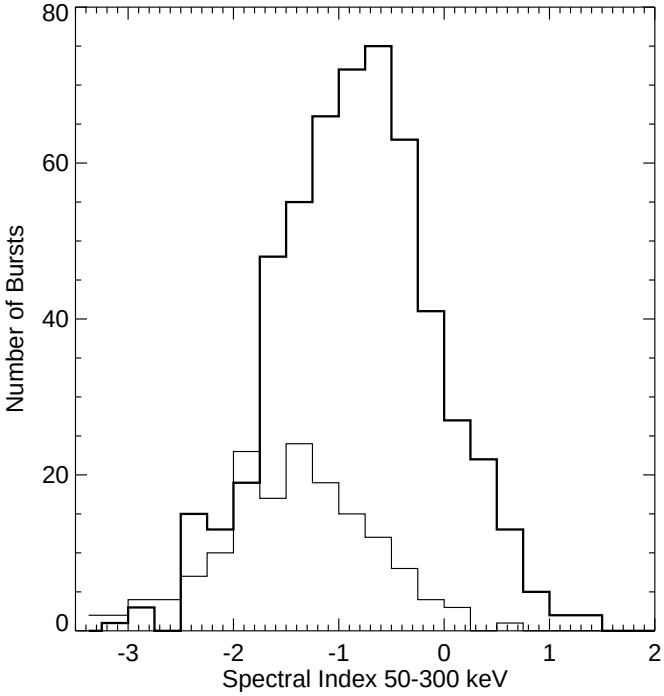

FIG. 7.—Spectral index distributions for 64 ms peak flux intervals for the HE bursts (*thick-lined histogram*) and the NHE bursts (*thin-lined histogram*).

so we should not expect hardness-intensity correlations to contribute significantly to the observed difference in absolute intensity. Still, we can explore this effect quantitatively by drawing subsets of bursts from the HE and NHE burst population in such a way that the subsets of each type of burst have identical spectral index distributions in the 50–300 keV peak flux interval. This is most easily done by selecting bursts of each type that have spectral index distributions like the intersection of the HE and NHE distributions. As can be seen from Figure 7, this includes almost all of the NHE bursts. The number of bursts selected in each spectral index bin was equal for the selected NHE and HE set. The HE bursts for this set were chosen at random by picking bursts sequentially in time from the beginning of the 3B burst catalog. In this way, a set of HE bursts was chosen that had a 50–300 keV spectral index distribution identical to the selected NHE set.

The intensity distributions for these sets on the 64 ms timescale are shown in Figure 8. The thick-lined histogram is the subset extracted from the HE bursts, and the thin-lined histogram is the NHE burst subset. The $\langle V_{\rm p}/V_{\rm plim}\rangle$ value for the HE subset is 0.344 ± 0.029. This is consistent with the first moment of the total HE burst set and deviates from homogeneity by 5.4 σ. The $\langle V_{\rm p}/V_{\rm plim}\rangle$ value for the NHE bursts is 0.53 ± 0.029, within 1.03 σ of homogeneity. The probability that the two data sets would differ by this much by chance is 6×10^{-6}. These results show that hardness-intensity correlations are not responsible for the homogeneity of the NHE bursts, since two sets with exactly the same spectral index distribution in the energy range where the intensity was calculated had significantly different intensity distributions.

The tests above indicate that the more obvious selection effects are not responsible for the homogeneous character of the NHE burst subset. The difference in luminosities

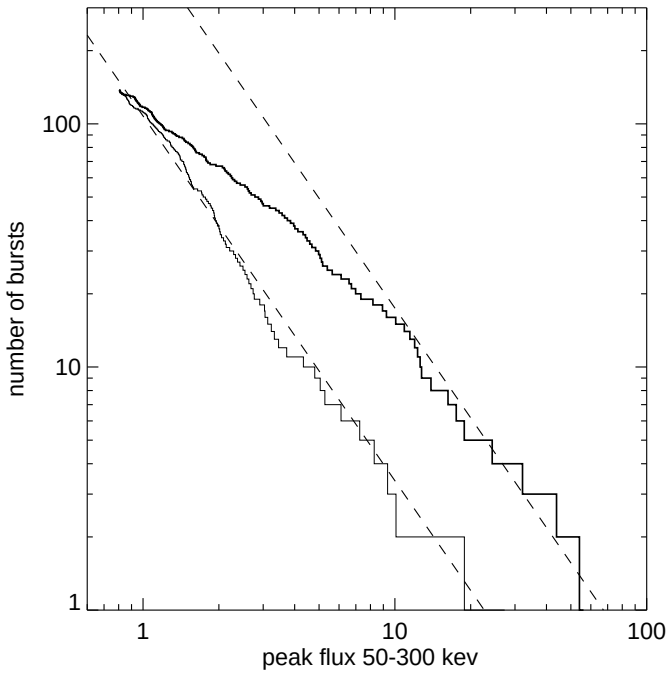

FIG. 8.—Intensity distributions for the two sets of bursts with identical spectral index distributions. *Thick-lined histogram:* HE bursts. *Thin-lined histogram:* NHE bursts.

between the homogeneous subset and the rest of the bursts is so strong, close to an order of magnitude, that the selection effects studied here are not capable of causing it. In the absence of any evidence supporting a selection effect origin for this burst subset's characteristics, we are left with the conclusion that it represents the true physical nature of the source object's burst dynamics.

5. FLUX HISTORIES OF BURSTS EXHIBITING BOTH HE AND NHE EMISSION

Without further study it might be natural to assume that the NHE bursts come from a set of objects distinct from those that produce the HE bursts. However, a closer examination of these two types of bursts reveals that the durations and complexities of the NHE bursts appear to be about as broadly distributed as those of the HE bursts. There are long ones, short ones, single-peaked, and multipeaked events of both types. In fact, the complexity and variability of the NHE bursts is such that it is generally impossible to distinguish them from HE bursts by examining their flux histories in the lower three channels.

We would have been more inclined to accept without further analysis the postulate that the NHE bursts were produced by a different source object than the one responsible for the HE bursts if, for instance, the NHE bursts had turned out to all be smoothly evolving events with only a few emission peaks of about the same duration, in contrast to the HE bursts. The data in Figures 2*a*–3*c* show that this is not the case. The morphological similarities between the HE and NHE bursts prompt us to examine them more closely. A study of the spectral properties of the emission within gamma-ray bursts reveals that both HE and NHE types of emission peaks can be found within a number of individual bursts, as is described in detail below.

It is clear from Figures 2*a*–3*c* that individual bursts are often composed of a number of emission peaks. Examination of the flux histories of the bursts shows that many bursts contain both HE and NHE peaks. Figure 9*a* shows the flux history for a double-peaked burst where the first peak is HE emission and second is NHE emission. Figure 9*b* shows a burst composed of a number of peaks with varying amounts of high-energy emission. The last peak in this burst is of the NHE type. In Figure 9*c* a double-peaked burst is shown that exhibits strong hard-to-soft evolution throughout its flux history. The burst appears double peaked in its 50–300 keV flux history, and this hard-soft peak doublet appears fairly frequently in GRB flux histories, although we have yet to perform quantitative analyses of this spectral structure. Although most of the softer peaks occur later in the bursts, there are exceptions to this behavior, as is seen in Figure 9*d*. This burst begins with a short NHE peak, the brightest peak in the burst, that is followed by HE emission later on.

These examples show that HE and NHE peaks occur simultaneously in the same bursts and therefore must be being produced by the same source object. Although there is some qualitative evidence that the two types of emission are related, and that the HE emission usually precedes the NHE emission, the peaks are also often quite distinct, indicating that the strength of the relationship between the two types of emission may vary from burst to burst. In any case, these burst flux histories raise the question: Are the spectral properties of the NHE peaks in HE bursts similar to the spectral properties of NHE peaks in NHE bursts? If the NHE peaks in both types of bursts appear to have the same properties, then both types of emission would appear to come from the same source object. This would mean that the homogeneous NHE burst set would simply represent a realization of the common gamma-ray burst emission mechanism where the HE emission was not observable by us. Therefore, it would not be evidence for another class of object, but would rather support a multiple spectral component source object as the source of all the gamma-ray bursts. To answer this question we present procedures for defining burst emission peaks in Appendix A and techniques for studying their spectral properties below.

6. THE DISTRIBUTION OF SPECTRAL INDICES FOR BURSTS AND FOR PEAKS WITHIN BURSTS

The topic of gamma-ray burst peak decomposition has been explored by various researchers (Norris et al. 1994; Davis et al. 1994; Lestrade et al. 1994). The complex morphology of the bursts makes the problem challenging and invites a variety of approaches. We have developed an approach here that identifies peak emission regions based on their statistical significance and their amplitude relative to the emission surrounding them. The technique is designed to break up the bursts into intervals where most of the emission within the interval is due to emission peaks that originated in that interval. The technique is described in detail in Appendix A.

The peak decomposition procedure was applied to 750 bursts for this analysis. For each peak interval identified, a number of observables were calculated including the peak fluxes on the three trigger timescales and spectral indices in the energy ranges 25–100, 50–300, and $E > 100$ keV for the peak flux intervals as well as the entire peak interval. This database permitted a quantitative search for NHE peaks in

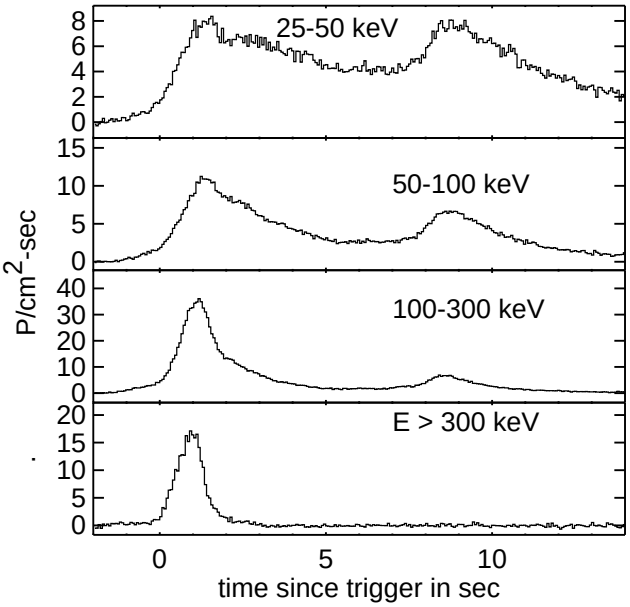

FIG. 9*a*

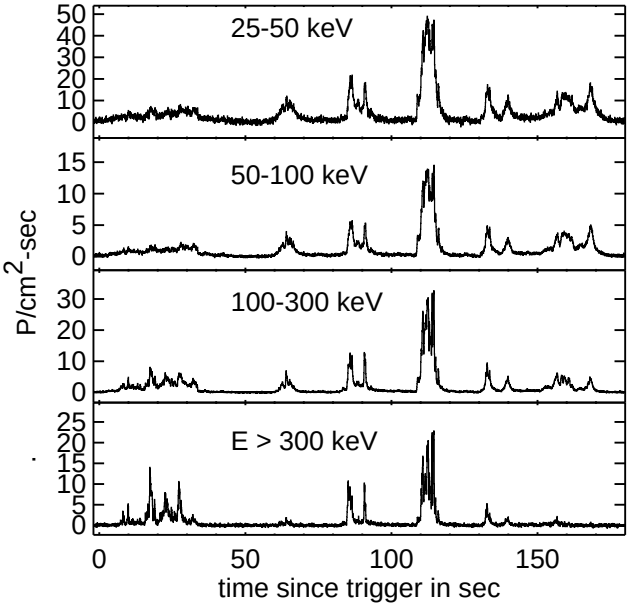

FIG. 9*b*

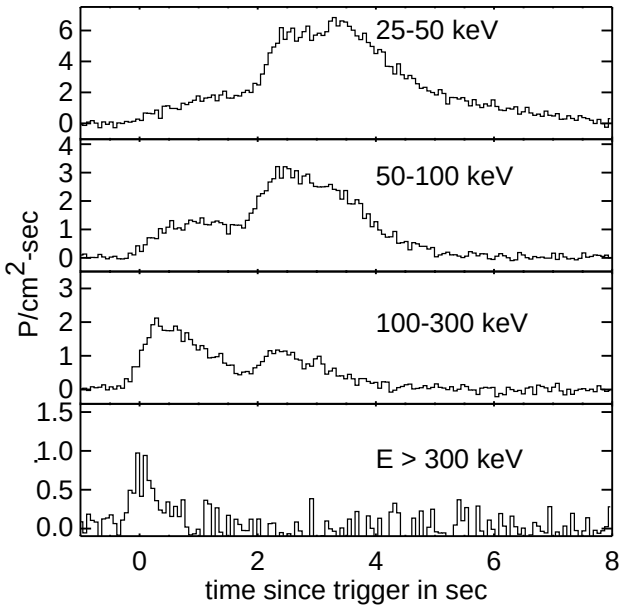

FIG. 9*c*

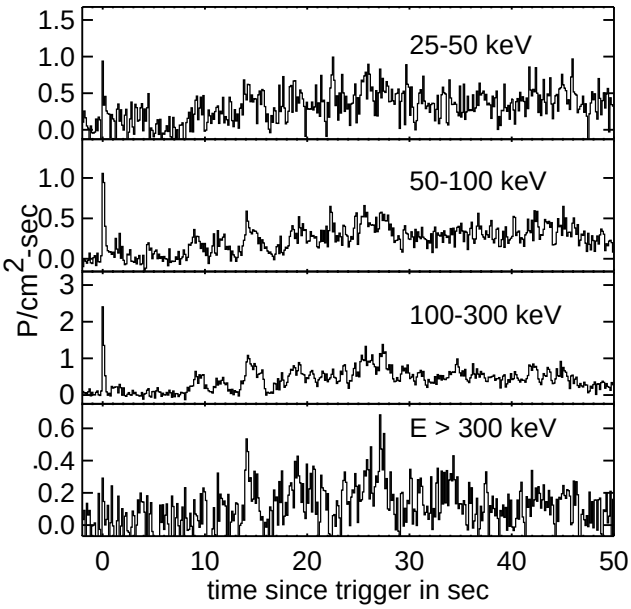

FIG. 9*d*

FIG. 9.—Flux histories for HE bursts containing NHE peaks are shown here in physical units of photons cm^{-2} s^{-1} with (*a*)–(*c*) 64 ms resolution and (*d*) 128 ms resolution. The four BATSE LAD discriminator channels are shown separately.

HE bursts and allowed for the comparison of their spectral properties with other peaks in bursts. To begin the spectral comparison of HE and NHE bursts, we will first examine the distributions of the total burst emission, or fluence, spectral indices. Figure 10 shows a scatter plot of fluence spectral indices for the high-energy bursts. The 50–300 keV spectral index is displayed on the horizontal axis and the $E > 100$ keV index on the vertical axis. The small diamonds on the plot show the actual values for each member of the HE burst population. A few of the points have error bars on them to illustrate their representative size. Plotting the entire distribution with error bars yields a confusing display that is not very informative. What we are trying to convey here is the general shape of the spectral index distribution for this set of bursts. The contours are fit to the data summed into square bins 0.5 spectral index units on a side.

Figure 11 shows the total burst emission spectral index distribution for the HE bursts, like it is shown in Figure 10, as a solid set of contours. Also shown here is the NHE burst distribution represented by dotted line contours. The $E > 100$ keV indices for this set are simply upper limits, so the contours are shown extending out of the plot and are considered unbounded on the lower side. What is of interest here is the extent of each distribution in the 50–300 keV range. The two distributions clearly cover different domains in this dimension.

We can now begin to address the question of whether or not the NHE peaks in HE bursts are similar to the NHE

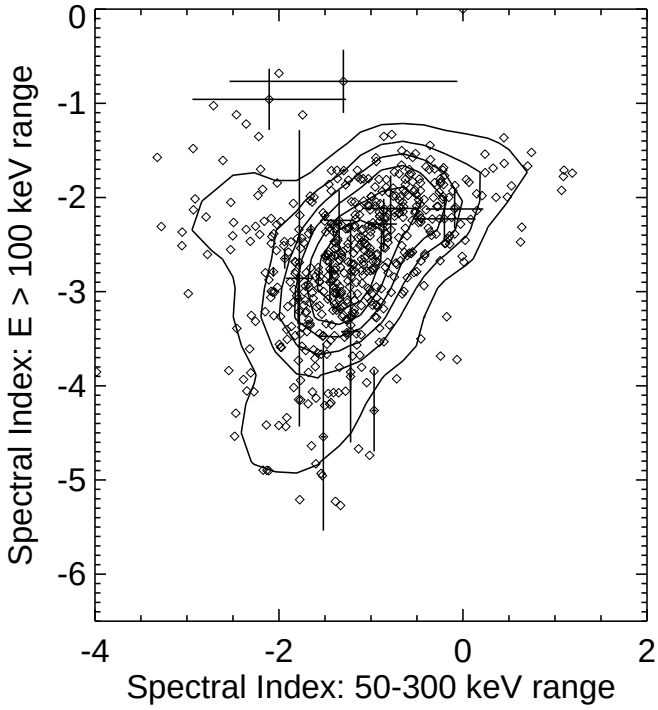

FIG. 10.—Scatter plot of the fluence spectral indices for the HE bursts with the 50–300 keV indices displayed along the horizontal axis and the $E > 100$ keV indices displayed along the vertical axis. The ensemble of small diamonds represents the total burst distribution. The crosses represent individual burst data points with errors. The closed, concentric lines represent a contour fit to the total burst distribution.

peaks in NHE bursts. Since we have decomposed the bursts into separate peak intervals as defined above, we can examine the spectral index distributions of the peaks within bursts in the same way as we have the total fluence spectral index distribution. For this analysis, the spectral index of the peak is calculated for all the flux within the peak interval so that it represents the spectrum of the peak's fluence. Figure 12 shows the spectral index distributions in the 50–300 keV range versus the $E > 100$ keV range for all the peaks in HE bursts as solid sets of contours. There is a set of HE peaks that has a distribution very similar to the HE burst fluence spectral index distribution shown in Figure 11. However, there is also a population of NHE peaks from the HE bursts shown as the set of solid contours at the bottom of the figure, and these peaks have a distribution quite similar to the NHE burst fluence distribution in Figure 11. Also shown in this figure is the spectral index distribution of all the peaks in NHE bursts represented by the set of dotted line contours. There are no HE peaks in this set; however, both sets of NHE peaks from the different bursts appear to have very similar distributions in this energy range.

In order to broaden the domain in which we perform our spectral comparison, we can examine the spectral index distributions of the peaks in the 25–100 keV range versus the 50–300 keV range. In Figure 13 the distribution for the HE peaks in HE bursts is shown as the set of solid contours. The dashed contours show the distribution for NHE peaks in HE bursts. The distributions overlap significantly, but they are distinctly different in both the 50–300 keV dimension and the 25–100 keV dimension. Figure 14 shows the distributions for the NHE peaks from HE bursts (*dashed contours*) and the NHE peaks from NHE bursts (*dotted contours*). These distributions overlap quite well and seem to have the same characteristics.

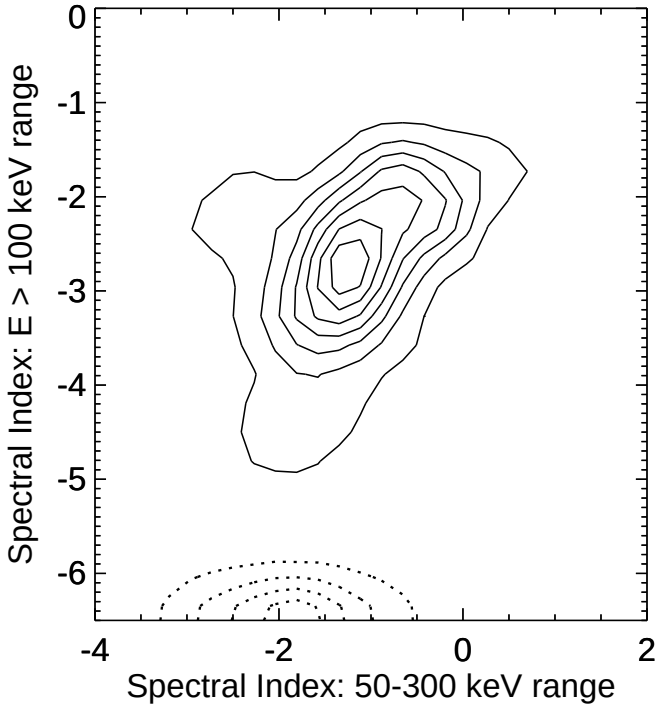

FIG. 11.—Scatter plot of the fluence spectral indices for the HE bursts (*solid lines*) and NHE bursts (*dotted lines*) with the 50–300 keV indices displayed along the horizontal axis and the $E > 100$ keV indices displayed along the vertical axis. The $E > 100$ keV indices are upper limits for the NHE bursts.

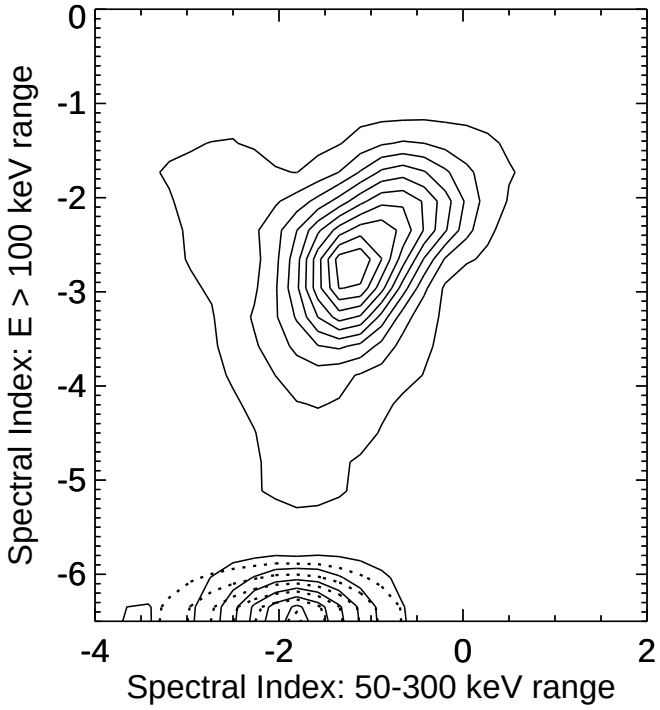

FIG. 12.—Scatter plot of the spectral indices for peaks within the HE bursts (*solid lines*) and NHE bursts (*dotted lines*). Here the HE bursts have two separate sets of peaks, one of which spans the same spectral range as the peaks from NHE bursts.

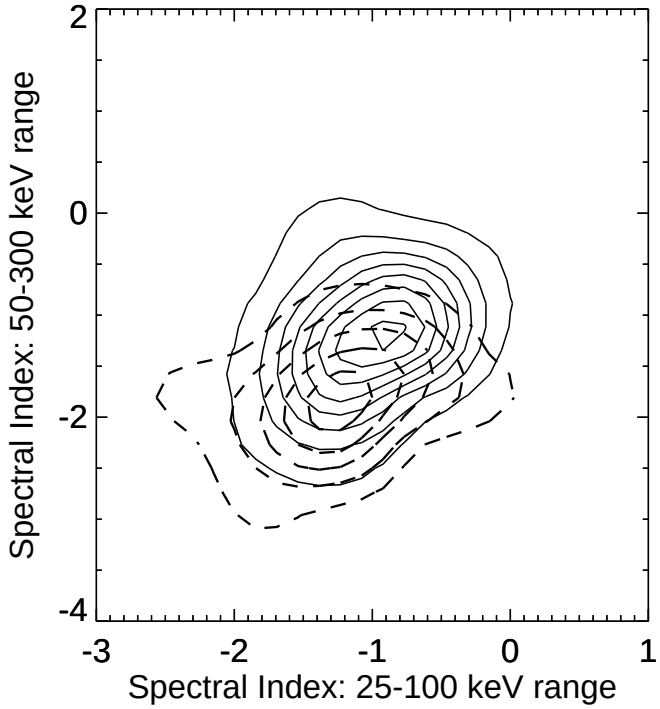

FIG. 13.—Scatter plot of the spectral indices for HE and NHE peaks within the HE bursts with the 25–100 keV spectral indices displayed along the horizontal axis and the 50–300 keV indices displayed along the vertical axis. *Solid lines:* HE peaks from HE bursts. *Dashed lines:* NHE peaks from HE bursts.

We can make quantitative statements about these distributions by comparing the data binned into histograms for each spectral index separately. Figure 15 shows these histograms normalized to unit area and compared with a χ^2 test. The upper left-hand panel shows the 25–100 keV index distribution histograms for the HE peaks from HE bursts (*thick-lined histogram*) and the NHE peaks from HE bursts (*thin-lined histogram*). Although these two types of peaks are from the same kind of bursts, their distributions are different, with a reduced χ^2 of 3.45 for 13 degrees of freedom with a chance probability of 2.1×10^{-8}. In this analysis, histogram bins were used if either distribution had bursts in that bin. The upper right-hand panel shows the distributions for the NHE peaks from HE bursts (*thin-lined histogram*) and the NHE peaks from NHE bursts (*thick-lined histogram*) in the 25–100 keV energy range. Even though these peaks are from different types of bursts, their distributions are consistent with a reduced χ^2 of 0.50 with 13 degrees of freedom for a chance probability of being similar of 93%. The lower left-hand panel shows the distributions in the 50–300 keV range of the HE peaks from HE bursts (*thick-lined histogram*) and the NHE peaks from HE bursts (*thin-lined histogram*). These distributions are clearly different with a reduced χ^2 of 19.5 for 14 degrees of freedom. However, the distributions shown in the lower right-hand panel of the NHE peaks from the HE (*thin-lined histogram*) and NHE bursts are much more similar with a reduced χ^2 of 0.91 with 10 degrees of freedom, for a chance probability of being similar of 52%. The distributions are remarkably similar for peaks coming from two potentially different kinds of burst, particularly when the peaks from within the same kind of burst can be so different. These results support the hypothesis that the NHE peak emission from the two different types of burst are actually produced by the same source mechanism.

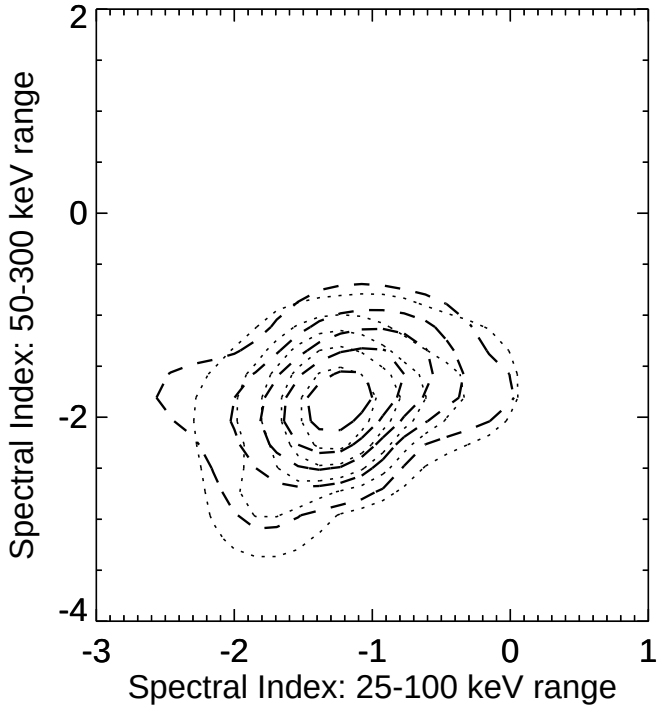

FIG. 14.—Scatter plot of the spectral indices for NHE peaks within the HE bursts (*dashed lines*) and NHE peaks within the NHE bursts (*dotted lines*) with the 25–100 keV spectral indices displayed along the horizontal axis and the 50–300 keV indices displayed along the vertical axis.

7. THE INTENSITY DISTRIBUTION OF NHE PEAKS WITHIN HE BURSTS

The existence of the burst data set decomposed into separate peak intervals allows us to run a test on the HE burst population where we restrict our observations of these bursts to only those intervals containing NHE peaks. We can apply this constraint and then calculate the intensity distribution for these bursts measured in this way. We will be observing these bursts as if we are sensitive to them only when they are producing NHE emission in isolation. If the NHE peaks in HE bursts are produced by the same mechanism as the NHE peaks in NHE bursts, then we might expect the results of this test to produce the homogeneous types of intensity distributions at lower intensities that we observed for the NHE bursts. We present this analysis, applied to the set of 750 bursts for which the peak analysis was performed, below. The intensity distributions, analogous to those shown in Figure 5 are shown in Figure 16. The numerical results, analogous to those shown on Table 2, are shown in Table 4.

In order to evaluate the results meaningfully, however, we need to consider the intensity-dependent selection effects that apply to bursts that can be decomposed into more than one peak. In the top panel of Figure 16 the upper thick-lined histogram shows the intensity distribution for the HE bursts that were analyzed using the peak decomposition technique. The upper, thin-lined, solid histogram that matches this thick one at higher intensities, but drops below it at lower intensities, represents those bursts that could be separated into two or more peaks. As we get to lower intensities, bursts are not decomposed into separate peaks as effectively. Of course, this is a fundamental limit for any

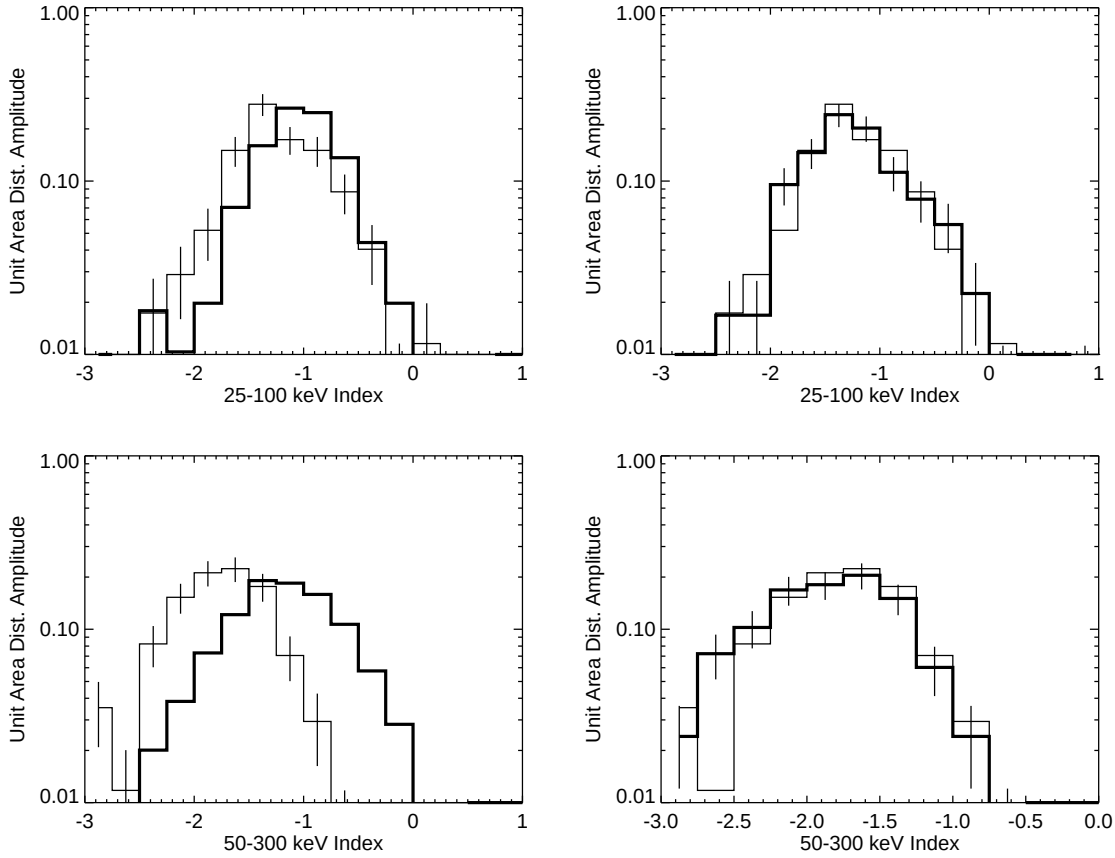

FIG. 15.—Histograms comparing spectral index distributions between the sets of bursts. *Upper left:* HE peaks from HE bursts (*thick-lined histogram*) and NHE peaks from HE bursts (*thin-lined histogram*) for the energy range 25–100 keV. *Upper right:* NHE peaks from HE bursts (*thin-lined histogram*) and NHE peaks from NHE bursts (*thick-lined histogram*) for the energy range 25–100 keV. *Lower left:* HE peaks from HE bursts (*thick-lined histogram*) and NHE peaks from HE bursts (*thin-lined histogram*) for the energy range 50–300 keV. *Lower right:* NHE peaks from HE bursts (*thin-lined histogram*) and NHE peaks from NHE bursts (*thick-lined histogram*) for the energy range 50–300 keV.

algorithm designed to recognize peaks based on their significance; below a certain intensity level, weaker peaks cannot be identified. Therefore, it is important to recognize this selection effect in any intensity distributions of burst subsets derived for the bursts identified as multipeaked.

TABLE 4

INTENSITY DISTRIBUTION PARAMETERS FOR HE AND NHE PEAKS FROM HE BURSTS

Quantity	64 ms	256 ms	1024 ms
1. HE_{min}	1.2	0.68	0.45
2. No. HE_{min}	193	219	216
3. $\langle V/V_{pcut}\rangle_{HE_{min}}$	0.27 ± 0.019	0.22 ± 0.016	0.16 ± 0.013
4. NHE_{thresh}	0.8	0.4	0.2
5. No. NHE_{thresh}	74	92	99
6. NHE exposure cutoff	1.2	0.65	0.33
7. No. NHE_{cut}	51	72	92
8. $\langle V/V_{pcut}\rangle_{NHE_{cut}}$	0.48 ± 0.041	0.40 ± 0.030	0.35 ± 0.028
9. DR_{low}	0.52–1.1	0.37–0.98	0.29–0.93
10. DR_{high}	0.92–1.9	0.41–1.1	0.32–1.0
11. LR_{low}	4.3–6.7	6.7–7.6	7 7.8–8.6
12. LR_{high}	8.9–14.0	18.3–20.9	23.1–25.7
13. LR_{bright}	8.32	7.98	8.27

NOTE.—HE_{min} = the larger of the lowest intensity multipeaked HE burst or the threshold in row (5) of Table 2. NHE_{thresh} = threshold for the NHE peaks within HE bursts. DR_{low} = ratio of the number of NHE to HE peaks within the homogeneous volume for HE volume lower edge. LR_{low} = luminosity ratio of HE to NHE peaks within the homogeneous volume for HE volume lower edge.

The $\langle V_p/V_{plim}\rangle$ value for the top thick-lined histogram is 0.344 ± 0.015, for a threshold value of 1.2 photons cm^{-2} s^{-1}, consistent with the total NHE burst distribution shown in Figure 5. The multipeaked intensity distribution (*thinner-lined histogram mentioned above*) has a significantly smaller $\langle V_p/V_{plim}\rangle$ value than that for total HE burst peak flux distribution, as can be seen in row (3) of Table 4, so we can expect some selection effects for weaker bursts. The lower, solid, thick histogram in the top panel of Figure 16 shows the 64 ms intensity distribution for the NHE bursts from the 750 burst subset analyzed here with $\langle V_p/V_{plim}\rangle = 0.520 \pm 0.029$, consistent with the NHE distribution of Figure 5, although representing a smaller set of bursts. The lower, solid, thin histogram in this panel is the intensity distribution for the HE bursts calculated using only the NHE peaks within those bursts. It has a $\langle V_p/V_{plim}\rangle$ value consistent with homogeneity despite the selection effects, as is shown in row (8) of Table 4.

This result supports the argument that the NHE peaks in both HE and NHE bursts come from the same source. In Figure 16, the homogeneity break ranges for the intensity distributions are delineated in the same fashion as they are in Figure 5. The NHE peak distributions all show homogeneity to low intensities, although the multipeak algorithm selection effects are expected to cause the first moments to be skewed to smaller values at lower intensities. The first moment values listed in row (8) of Table 4 show that this selection effect is most likely present at the lowest inten-

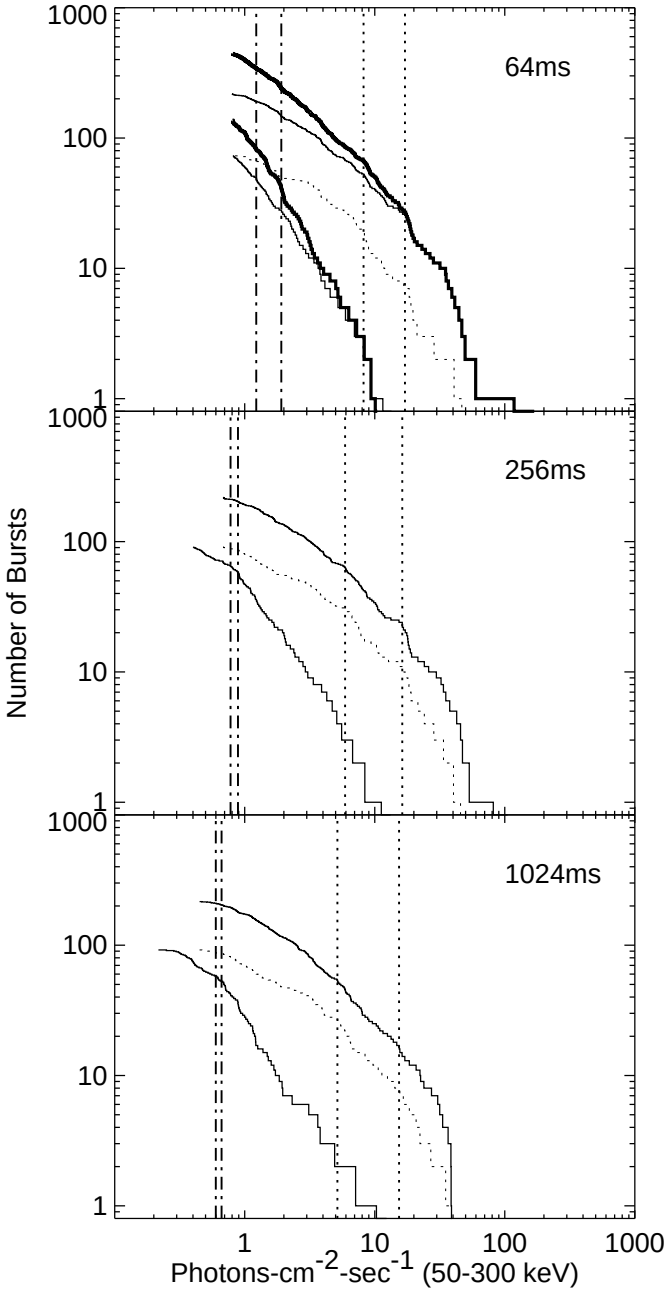

FIG. 16.—Peak flux intensity distributions on the BATSE trigger timescales for the data analyzed with the peak decomposition algorithm. *Upper thick-lined histogram:* All HE bursts (*top panel only*). *Upper thin-lined histogram:* Multipeaked HE bursts. *Lower thick-lined histogram:* All NHE bursts (*top panel only*). *Lower thin-lined histogram:* NHE peaks within HE bursts. *Dotted histogram:* HE peaks of bursts contributing to the lower thin-lined histogram. The dotted vertical lines show the intensity range where the HE distributions break from homogeneity. The dashed vertical lines show the intensity range where the NHE distributions break from homogeneity.

sities. The selection criterion for the NHE peak flux distribution was the brightest interval during NHE emission in an HE burst, which is a different criterion from the brightest interval in the burst regardless of spectral characteristics. In most cases the HE peak was brighter than the NHE peak, but this was not true in all cases. It is important to explore how adding a constraint to the peak flux selection process can affect the shape of the resulting distribution. This is explored in detail in Appendix B, where it is shown that the added selection criterion do not, in general, significantly change the intensity range where the break from homogeneity takes place in the observed distributions.

The density ratios of the NHE peak measured bursts to the total bursts within the homogeneous volume are given in rows (9) and (10) of Table 4. These values are calculated in the same way as the values in rows (11) and (12) of Table 2. In this case the number of HE bursts with NHE peaks in the homogeneous region is generally less than the total number of HE bursts in the homogeneous region. This is expected since we presume that the bursts with NHE peaks come mostly from the homogeneous region. As we will see below, there are probably effects based on the width of the NHE luminosity function that make the number of NHE peak bursts for the homogeneous region appear to be larger than it actually is, using the density ratio calculation.

The ranges of the luminosity ratios for the NHE peaks to the brightest peaks within HE bursts, calculated using the intensity distribution break ranges, are given in rows (11) and (12) of Table 4. These values are rather large, indicating a difference between the average luminosity of HE and NHE peaks of about an order of magnitude, like those given in rows (13) and (14) of Table 2. In fact, we might have expected the multipeaked algorithm selection bias against weak bursts to put the NHE break range at a considerably higher intensity, making the Table 2 and Table 4 results significantly more discrepant.

Figure 17 shows scatter plots of the HE peaks and NHE peaks used in Figure 16. One of the most obvious features in these plots is that the luminosity functions of the NHE and HE emission peaks are fairly broad, since the HE and NHE peaks values are not clustered along a line of fixed ratio. Also, at first glance, the data here could be interpreted as showing that the HE peaks are, on average, only about 4 or 5 times as bright as the NHE peaks. However, a closer examination of the data indicates that something else is going on. The upper diagonal line in these plots shows where the HE value equals the NHE value. The lower diagonal line shows where the HE value equals the NHE value times the luminosity ratio shown in row (13) of Table 4. This ratio is calculated by averaging the brightest 20 bursts from the HE intensity distribution (*upper solid-lined histograms of Fig. 16*) and dividing by the average of the 20 brightest bursts from the NHE peak distribution. In Figure 17 the brighter HE peaks are clustered around the lower diagonal line, indicating a significant difference between the average HE and NHE peak amplitude. However, the dimmer HE peaks are clustered around the upper diagonal line, indicating that for dimmer HE bursts the HE to NHE peak ratio is closer to one. This means that the HE to NHE peak ratio is a function of intensity in this data.

This observation is a fairly obvious result of the presence of somewhat broad HE and NHE luminosity functions and the instrument threshold. Far above the instrument threshold, we are likely to see most NHE peaks if they are present in an HE burst. Near the threshold, however, we are more likely to see an NHE peak in an HE burst if it is at the bright end of the NHE peak luminosity function. Therefore, we expect an intrinsic bias in the data we have selected here. We examine this directly in Figure 18, where we have taken the HE bursts with NHE peaks above threshold and ranked them by their brightest HE peak. Then we have grouped the bursts into sets of four and calculated the average ratio

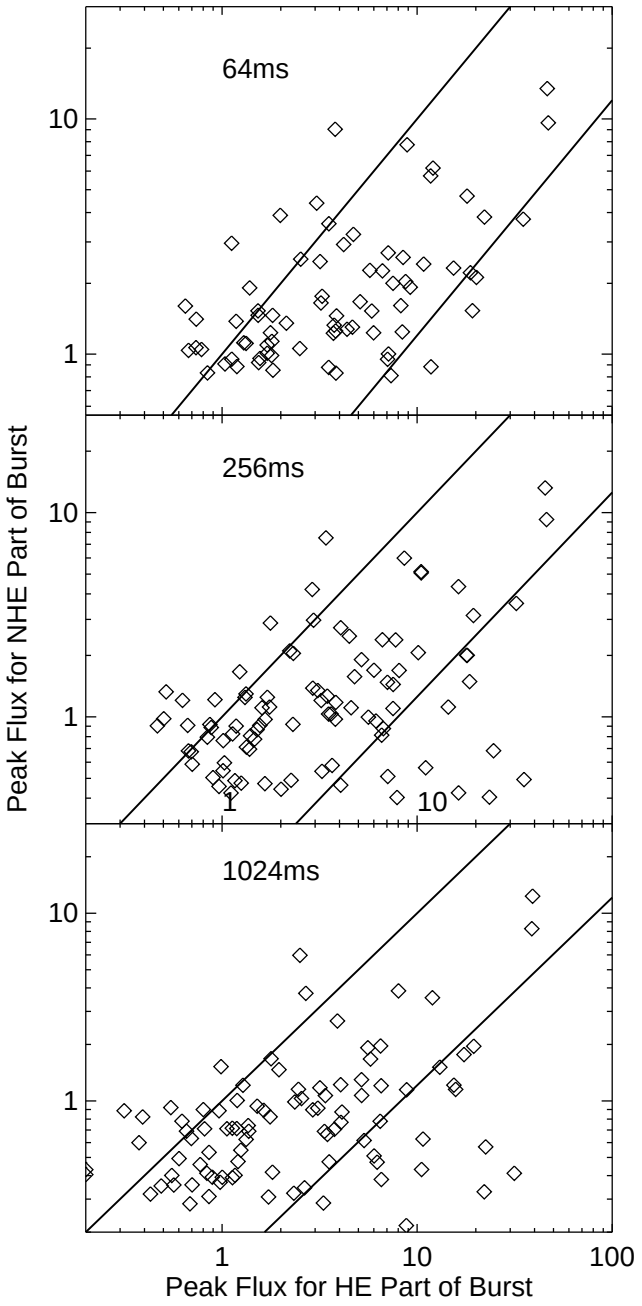

FIG. 17.—Distribution of peak fluxes on the three BATSE trigger timescales for bursts with both HE and NHE peaks above threshold. *Horizontal axis:* Peak flux from intervals with HE flux. *Vertical axis:* Peak flux from NHE intervals. The diagonal lines represent constant ratios between the two peak fluxes.

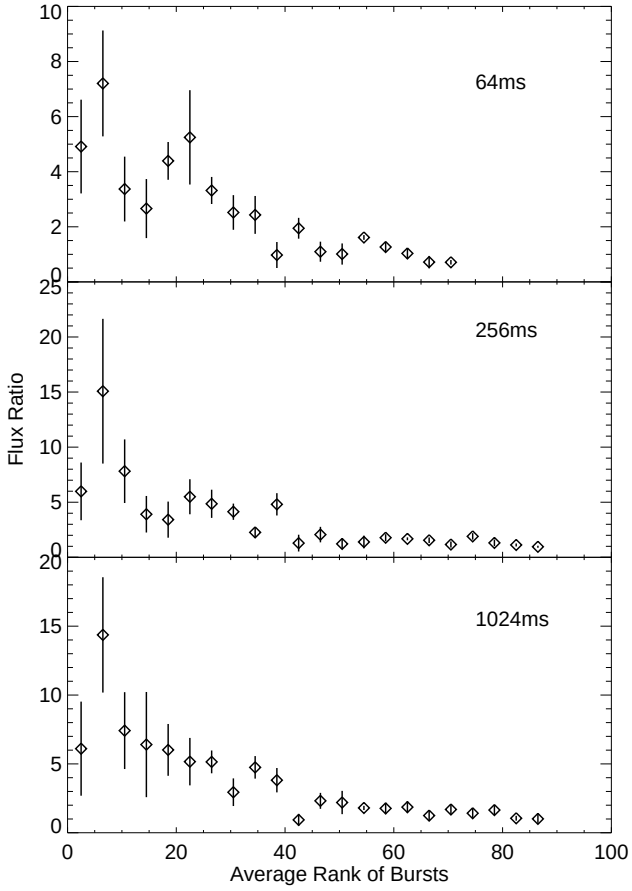

FIG. 18.—Distributions of ratios of HE peak intensities to NHE peak intensities on the three BATSE trigger timescales. HE bursts with NHE peaks are ranked by their HE peak intensity. The HE to NHE ratios are calculated in sets of four. Low rank number is associated with high intensity.

between their HE peak rate and their NHE peak rate. In this case the HE and NHE peak fluxes are being compared directly within each burst. The brighter bursts (with the lower rank indices) have high HE/NHE peak flux ratios, which are fairly consistent with the luminosity ratios in Tables 2 and 4. For the fainter bursts, the NHE peaks become brighter relative to the HE peaks. At the faintest end, the NHE peaks are, on average, brighter than the HE peaks. This is what we might expect with the broad luminosity function scenario described above.

This intensity-dependent sampling bias might explain why the NHE homogeneity break ranges in Figure 16 appear at the low intensities that they do. In Figure 16 we also show as dotted histograms the distributions for the peak fluxes calculated for the entire HE burst interval, for those bursts that contained NHE peaks above threshold. These bursts have been selected for the presence of an NHE peak, so we can expect some selection biases toward fairly bright NHE peaks relative to the HE peaks represented by the dotted histogram intensity distributions. Those distributions bend over, indicating that bursts from more distant regions of space, where they are not homogeneous, are contributing to the dimmer end of the NHE intensity distributions. Part of the lower intensity end of the apparently homogeneous region of the NHE distributions in Figure 16 may be caused by a sampling of the bright end of the NHE luminosity distribution out to distances beyond the region where the bursts are actually homogeneous. This effect may explain why the multipeak algorithm bias against weak bursts does not affect the density and luminosity ratios in rows (11)–(13) of Table 4 more strongly. The number of NHE peaks in the homogeneous part of the distributions on Figure 16 may be enhanced by the luminosity function selection effect described above.

The ratio of the brightest 20 of each type of peak (row [13] in Table 4) may be the least biased estimate of the average luminosity ratio. This ratio does not suffer from the possibility that the two distributions are drawn from sets of different sizes, like the ratios in row (15) of Table 2. In this

case all these peak fluxes come from exactly the same burst set. Nor does the HE peak flux distribution suffer from any precondition about the existence of an NHE peak in the bursts, like the peak fluxes in the dotted histograms, which could have a significant selection effect. This measure of the luminosity ratio may be the least subject to systematic error.

8. DISCUSSION

In §§ 2–4 we established the existence of the NHE bursts and showed that their intensity distribution exhibits homogeneity to much lower flux values than the HE bursts. The tests indicate that the homogeneity is in fact a physical property of the NHE burst subset and that it is not a consequence of selection effects. The simplest explanation for homogeneity of the NHE burst subclass is that these burst are so intrinsically faint compared with the HE bursts that we can only see the nearby ones that are distributed homogeneously.

These results considered in isolation might lead one to conclude that the gamma-ray burst population actually consists of two entirely different types of astrophysical objects, one with a significantly lower intrinsic luminosity than the other. However, the analyses in §§ 5–7 show that the same type of emission that characterizes the peaks in the NHE bursts can be found in the HE bursts. The NHE peaks in both HE and NHE bursts have the same spectral index distributions in both the 25–100 keV and 50–300 keV energy ranges. These distributions differ significantly from those of the HE peaks. It is surprising that the NHE peaks from the two different types of bursts have more in common than the HE and NHE peaks from within the same HE type bursts. Also, when the HE bursts' peak flux is measured using only NHE peaks within HE bursts, a more homogeneous intensity distribution is observed that is similar to the intensity distribution of the NHE bursts. This rather extensive set of comparisons strongly supports the position that the NHE emission is produced by the same physical mechanism in both the HE and NHE bursts. It seems most likely, then, that a single astrophysical object is capable of producing both types of spectral emission and that it frequently does. Sometimes, however, only the less luminous emission is observed resulting in the NHE bursts.

The evidence presented here indicates that the NHE emission is, on average, about an order of magnitude weaker than the HE emission in the 50–300 keV range. Although there are selection effects that should skew the ratios to larger values for some of the tests (Table 2) and to smaller values for other tests (Table 4), the luminosity ratios between HE and NHE peaks are reasonably consistent for all the tests performed here. More accurate estimates of the luminosity ratio will be possible with a larger data set. Also, modeling of the luminosity and spatial distribution functions, as well as the statistics of data collection, will improve the accuracy of our luminosity ratio estimates by allowing us to effectively assess the impact of selection effects on the measurements. The density ratio calculations are sensitive to selection effects as well, and detailed modeling will be important for verifying the hypothesis that the observed NHE bursts are actually more numerous per unit volume than the HE bursts, as the values in rows (11) and (12) of Table 2 suggest.

One can envision various scenarios consistent with these observations. One is that there are two distinct and unrelated emission mechanisms with narrow and well-separated luminosity functions. Another is that a single mechanism produces the NHE emission with low luminosity and that the emission transforms in a continuous, monotonic fashion to HE emission as the luminosity increases. The present analysis of the HE and NHE peaks within HE bursts suggests that the actual situation lies somewhere between the two cases described above. Both types of emission seem to exhibit fairly broad luminosity functions in that sometimes, within single bursts, the NHE emission is much weaker than the HE emission and other times they are about equal in strength. The large scatter in the points in Figure 17 is evidence for this. A single mechanism with a monotonic spectral-luminosity function would not produce this scatter. Also, since NHE bursts do not show HE emission, there appear to be bursts that, from our point of view, stay only at the NHE level. Therefore, if we are observing one mechanism that evolves between HE and NHE states, it certainly does not do so in all cases. On the other hand, the NHE and HE emissions appear frequently to be mixed together, so that some causal relationship between the two may well exist. In the time interval from 16 to 19 s in Figure 2*a*, there is HE emission decaying smoothly away with time. Superposed on top of this is a pulse of NHE emission. In this case, although the emission is obviously superposed, the HE emission seems unaffected by the presence of the NHE emission, as is evidenced by the smooth decline in flux in the $E > 300$ keV range during this interval. As we noted in Figure 9*c*, however, the HE and NHE flux seem frequently to be coupled together somehow. These phenomena make it difficult to say exactly how coupled or separate the two types of observed emission are. The two types of emission may occur together most of the time. A larger data set will allow us to break the bursts up into differential bins of high-energy spectral index with statistically significant samples of bursts in each bin, so that we may study the intensity distributions as a function of high-energy hardness more precisely.

These observations do indicate that there are quite distinct forms of spectral emission occurring in single burst sources and that source mechanisms capable of producing both types of emission must be invoked to explain it. These mechanisms could take the form of a single type of emission site that evolves in some continuous fashion between distinctly different emission modes or two different emission sites that are dynamically coupled to each other, yet produce different high-energy spectra.

If the density of NHE bursts does turn out to be greater than that of HE bursts, this could be explained in a variety of ways. One possibility is that the more luminous HE emission is beamed into a smaller solid angle than the NHE emission. In this case we would observe a higher density of NHE bursts. Another alternative is that the two types of emission are produced isotropically or are beamed into about the same solid angle, but bursts tend to produce NHE emission in isolation more frequently. If the two types of emission are beamed, then their beaming axes may not be aligned. In this case we would see a variety of bursts with various mixtures of the two types of emission. The beaming factor could vary from burst to burst for each type of emission, even if the average beaming factors for the two kinds of emission are significantly different. Further spectral studies will be necessary to learn more about the admixture of HE and NHE emission.

9. SUMMARY

We have presented here a sizable body of evidence that supports the theory that bursts are composed of significantly distinct HE and NHE spectral emission states. The HE emission appears to be about an order of magnitude brighter than the NHE emission, a difference large enough to be strongly manifested in the burst intensity distributions. It is also shown that one source object is capable of producing both types of emission, so bursts with only NHE emission do not represent a different class of astrophysical object, but one manifestation of the mechanism common to all gamma-ray bursts. These developments in the study of gamma-ray burst behavior, particularly their spectral behavior, are important for the quantitative characterization of the tumultuous burst phenomenon. The identification of distinct spectral components in gamma-ray bursts with significantly different luminosities is an important clue in the search for the elusive source of these enigmatic events, a topic that has become one of the great unsolved scientific mysteries of our time.

APPENDIX A

ANALYSIS TECHNIQUES FOR PEAK IDENTIFICATION AND SPECTRAL DATABASE PRODUCTION

We outline here a technique developed for the decomposition of gamma-ray bursts into separate peaks to support the study of the global population spectral characteristics of the bursts. For this method we have chosen to define an emission peak in a burst flux history in the following way: an interval where the burst flux first rises by 5 σ and then falls by 5 σ is defined as an emission peak.

This particular definition has the advantage that it does not depend on any particular peak shape or duration definition, and it will not be foiled by statistical fluctuations. By defining the existence of a peak in statistical units, we can control the identification of false positives and push the technique to the lowest practical intensities. The technique that is outlined here is described in detail elsewhere (Pendleton et al. 1997) and is probably overkill for this application. Since it is used here, however, this method will be briefly described.

The top panel in Figure 19 shows the flux history for burst 3B 940217, also shown in separate energy bands in Figure 9*b*, for the energy range 50–300 keV with 64 ms resolution. The statistical error in the flux, σ, is calculated from a polynomial fit to the errors in this flux data versus its intensity. Then the flux history is digitized in units of σ in the following manner. The flux history is converted into $\frac{1}{3}$ σ level units starting from a flux value of zero. Converting the flux history from photons to $\frac{1}{3}$ σ units instead of, say, 1 σ units avoids the problem of having a particular significant peak out of phase with the significance level quantization. Digitization at the $\frac{1}{3}$ σ level is sufficiently continuous to permit the identification of significant peaks with reasonable consistency.

At this point the digitized history is still expressed in real number form and looks almost like the flux history as it is shown in the second panel of Figure 19. The flux history, however, is further processed to include some information about the rate of change of the flux around each time bin edge. To accomplish this, a $\frac{1}{3}$ σ value is assigned to each time bin edge, based on the values of the flux in the bins on either side of it. If the flux in the later bin is higher than in the earlier bin, then the value assigned to that bin edge is the positive $\frac{1}{3}$ σ level just below the later data. This value marks the bin edge as one where the flux increased to a particular significance level: the rate of change of the flux was positive. If the flux in the later bin is lower than in the previous one, the $\frac{1}{3}$ σ level just above the later data is assigned to that bin edge with a negative sign in front of it. The negative sign indicates that the rate of change in the flux around this bin edge was negative. This procedure results in the digitization of the flux history in units of statistical significance. The time axis is replaced with time bin edge index values, and the flux is replaced with values quantized at $\frac{1}{3}$ σ significance, also marked with a positive or negative sign to indicate the rate of change of the flux at that time. The digitized flux history shown in the second panel of Figure 19 shows the absolute value of these $\frac{1}{3}$ σ values versus the time bin edge indices.

This panel also shows some 2 σ flux intervals delineated with trapezoidal boxes. The base of the trapezoid spans the interval where the flux is greater than or equal to a particular base flux level. The top of the trapezoid spans the interval where the flux is greater than or equal to the base flux level plus 2 σ. These trapezoids were constructed for the purposes of rebinning the less intense data and not for identifying 2 σ peaks, but they can be used as an example of how the trapezoidal identification procedure works.

We will use here as an example of the method of searching for trapezoids the case where we want to construct trapezoids that specifically delineate intervals where the burst flux rises from below 2 σ to above 4 σ and then drops back down again. In this case our base flux level in $\frac{1}{3}$ σ units is 6 and our peak flux level is 12. The first task is to find an interval where the flux rises from 2 σ to 4 σ. We start searching through the digitized flux history sequentially looking for a digitized flux value of $+6$ or greater. When we find one, we store the time bin edge index and then continue the search, now looking for a value of $+12$ or greater. If, however, we find a value of -6, or a negative value with smaller absolute value, before we find a value of $+12$ or greater, then we discard the first $+6$ time bin edge index and start the search anew. We do this because we are trying to identify an interval where the flux rises from 2 σ to 4 σ without dropping to 2 σ in the mean time. This will introduce a bias toward slightly narrower peak rise fronts; however, it ensures that the rise front identified has the desired significance, in this case, at least 2 σ. Once a trapezoid rise front has been confirmed by finding a value of $+6$ or greater followed by a value of $+12$ or greater without any intervening -6 values, then the time bin edge indices are stored, and the search now shifts to the identification of trapezoid falling interval.

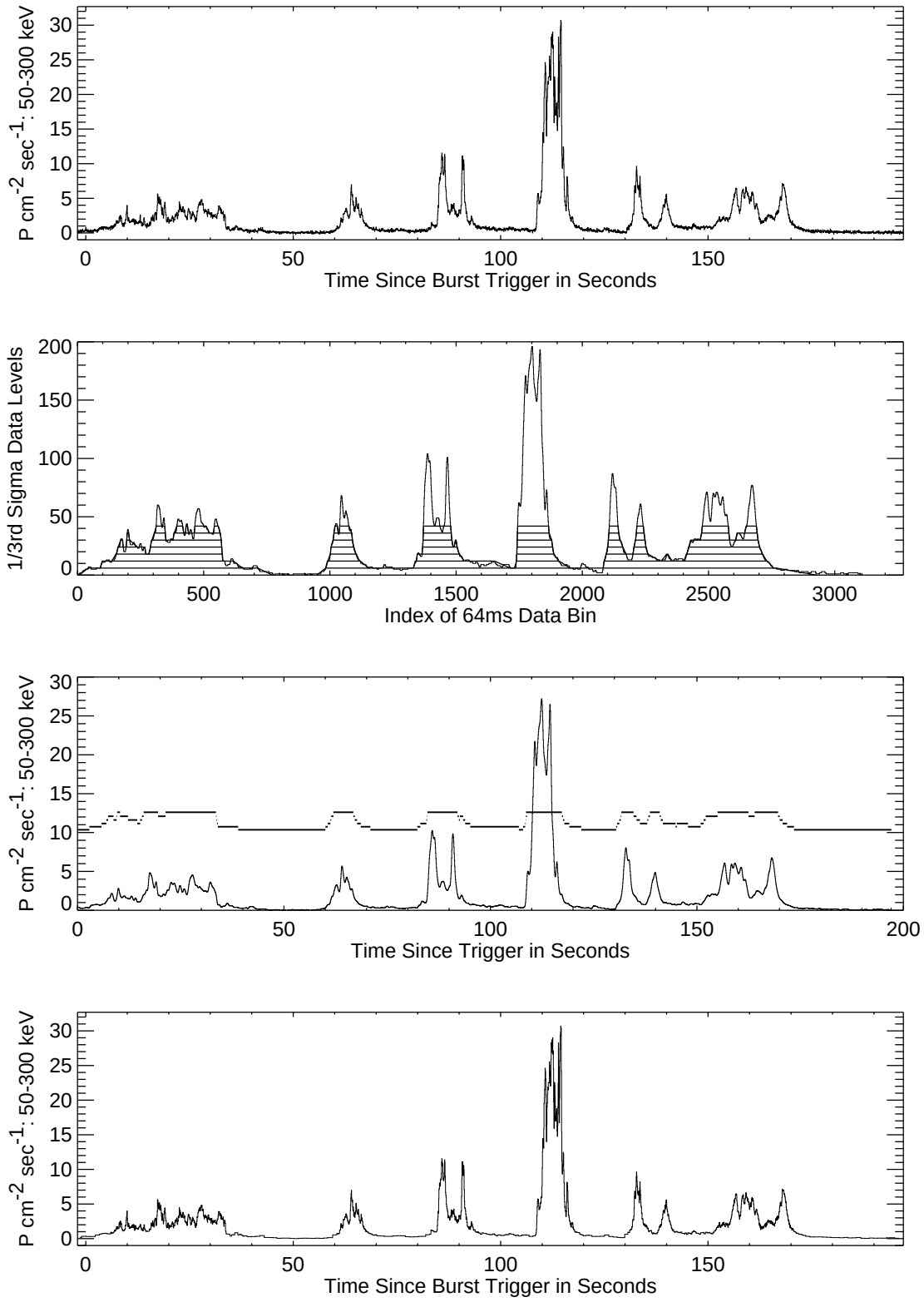

FIG. 19.—*First panel:* Flux history for BATSE trigger 3B 940217 with 64 ms resolution. *Second panel:* Digitized flux history for 3B 940217 with 2 σ trapezoidal flux envelopes at lower intensities. *Third panel:* Flux history with rebinning intervals superimposed. *Fourth panel:* Flux history rebinned at lower intensity in the intervals shown in the third panel.

In the falling interval search, the first target value is -12, or a number with an absolute value smaller than this, indicating that the flux has dropped below the 4 σ level. When this value is found, the search continues for a -6 or a number with a smaller absolute value. If a $+12$ or greater is encountered in the meantime, then the -12 search is stared again. This procedure finds the 4–2 σ falling interval completing the trapezoid identification. We have four time bin edge indices, and the

base and top level values used in the search to define the trapezoid. These trapezoid bases can be statistically biased toward shorter intervals, so they are not particularly appropriate for duration versus intensity studies. However, they are adequate for coarse population distribution characterization.

The results of the 2 σ peak identification in the example above were used for rebinning and not for actual burst peak identification. As stated above, a 5 σ threshold was used for actual peak identification. With the data binned on the 64 ms timescale, however, less intense features are not measurable at the 5 σ level, particularly the long, less intense emission characteristic of some of the hard-to-soft evolving peaks. We can push the technique to lower flux levels at the expense of temporal resolution by binning the data more coarsely in time during intervals where the flux was below 8 σ.

It is useful to define some terms for illustrating the application of the trapezoidal decomposition technique. The trapezoid peak interval is defined by the start and end points of the upper horizontal part of the trapezoid, i.e., the duration of the top of the trapezoid. The trapezoid base interval is defined by the start and end points of the lower horizontal part of the trapezoid, i.e., the duration of the bottom of the trapezoid. The trapezoid rise interval or rise front is defined as the interval bounded by the beginning of the base interval and the beginning of the peak interval. It is generally shown in the figures with a slanted line with positive slope connecting the front of the peak and base intervals.

To identify the intervals appropriate for rebinning, the trapezoidal decomposition technique described above was applied to the $\frac{1}{3}$ σ flux history digitization at 2 σ levels starting at the zero flux level. The digitized flux history is shown in the second panel of Figure 19. Here the $\frac{1}{3}$ σ flux levels are shown with the negative signs removed for clarity. Superposed on the digitized flux history are the trapezoidal decompositions of the data calculated at 2 σ level intervals, which are separated by a factor of 6 in these units. Only the lowest seven 2 σ decompositions are shown (i.e., those decompositions closest to zero), and only the lower 4 of these are currently used for rebinning. The actual flux history time intervals for rebinning are selected by subtracting the base intervals of the trapezoids at a particular 2 σ level from the base intervals of the trapezoids from the 2 σ level directly below. The third panel of Figure 19 shows the flux history of the burst with the time intervals for the different flux intensity levels superposed and shifted vertically by 10 photons cm^{-2} s^{-1}. The data in intervals with flux above 8 σ remained at the original 64 ms resolution. The data in the intervals where the flux was between 6 and 8 σ were rebinned by 2. Intervals in the 4–6 σ range were rebinned by 3. Data in the 2–4 σ range was rebinned by 6 and in the 0–2 σ range by 16. The bottom panel of Figure 19 shows the rebinned data for this burst. The lower intensity intervals exhibit less statistical fluctuation than in the top panel.

With the data rebinned, the statistical error, σ, versus intensity can be recalculated and the trapezoidal decomposition applied again. At lower intensities the significance levels are now more closely spaced in physical flux units, so that significant 5 σ peaks can be found at lower intensity values. For the actual peak decomposition, 5 σ trapezoids are identified at all of the $\frac{1}{3}$ σ levels. The general result is a set of nested trapezoids, separated by $\frac{1}{3}$ σ in intensity. Our objective is to reduce this representation to a single unique set of trapezoids like that shown in Figure 20. To do this, we take each trapezoid base and peak interval, then we check to see if there are any trapezoid base intervals identified at this particular trapezoid's peak level

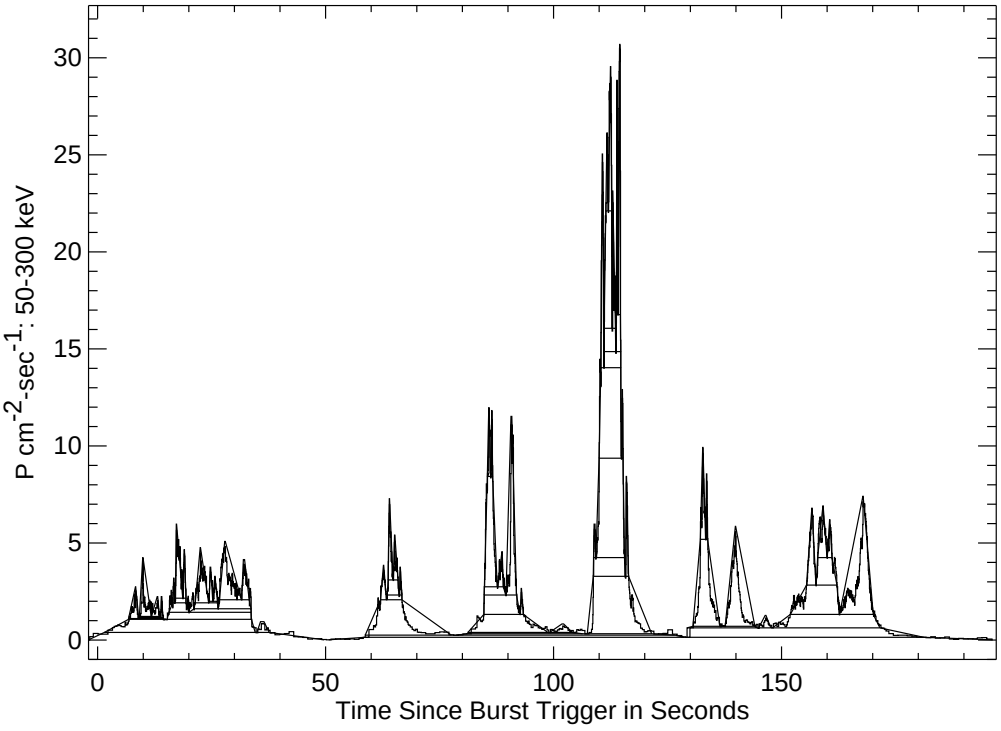

FIG. 20.—Trapezoidal decomposition of 3B 940217. The thin line is the rebinned flux history, and the thick lines are the trapezoids enclosing the significant peaks in the burst.

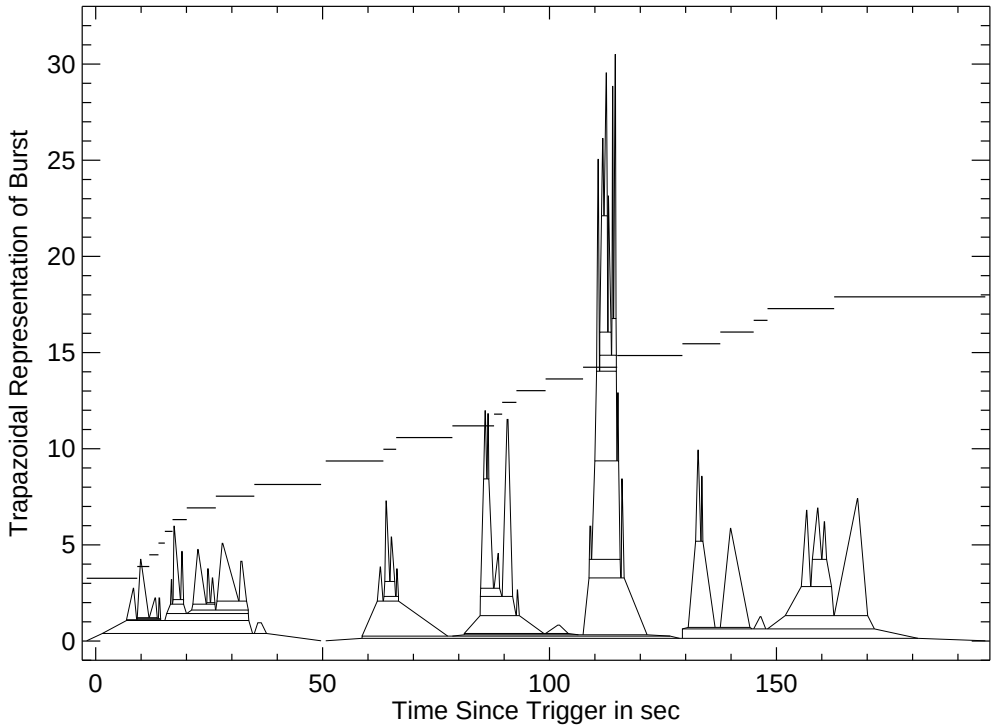

FIG. 21.—Trapezoidal decomposition of 3B 940217 (*thin lines*) with the peak interval selections superposed (*thick lines*)

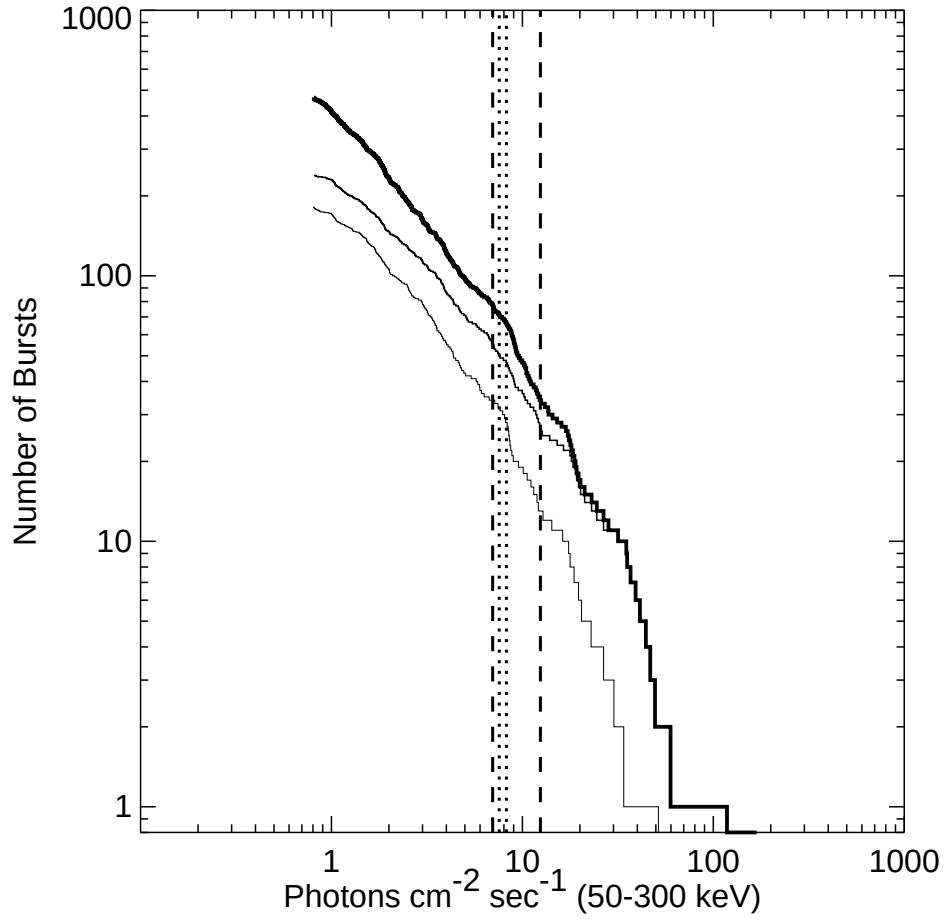

FIG. 22.—Peak flux intensity distributions on the 64 ms timescale for the data analyzed with the peak decomposition algorithm. *Upper thick-lined histogram:* All HE bursts. *Upper thin-lined histogram:* Multipeaked HE bursts. *Lower thin-lined histogram:* Peaks with 50–300 keV spectral indices in the range -3 to -1 within HE bursts.

that are contained within its peak interval. If not, we replace the current trapezoid's peak interval by the peak interval of the trapezoid shifted $\frac{1}{3}\ \sigma$ up from the current one. We continue this process until we find some 5 σ peaks contained within the current trapezoid's peak interval. When this happens, we seal off the current trapezoid, and then continue the process with any remaining ones above the current level. This process decomposes the flux history into trapezoidal sections that show where the flux can be separated into distinct peaks that are statistically significant and also indicates were the flux is merged together too much for separation at the significance level used to define the peaks. In Figure 20 there are a number of triangular, or nearly triangular, trapezoids identified that represent significant peak emission. However, many of these trapezoids are sitting on other trapezoids that are closer to rectangular in shape and represent regions where the flux cannot be clearly separated into distinct emission peaks. The emission peak morphology of this burst is clearly quite complicated and defies a simple definition of peak emission for the separation of the peaks. A fairly large number of bursts exhibit this kind of complex peak morphology.

In order to do a comprehensive and complete study of the burst spectral properties, it is desirable to select a definition of peak emission that allows us to make use of all the burst flux. To achieve this, we separated the bursts' flux histories into consecutive intervals containing flux that primarily originated inside the intervals. The trapezoids are examined in generally ascending order in terms of their peak level values. The first interval starts at the beginning of the flux history. Then, for a given trapezoid, the peak level value in physical units is compared with the highest peak flux value inside the peak interval. If the peak level value is 33% or more of the peak flux value, then an emission interval is identified. If the trapezoid in question is at the peak flux level, then its base-to-peak amplitude must also be 33% of the peak flux. This additional constraint avoids the selection of small peaks on the rise fronts of large emission intervals, like the small peak at 110 s in Figure 20. Once a peak interval trapezoid has been identified, then the remaining trapezoid list is searched to find when the next rise interval occurs after the current trapezoid's base interval. The start of this next rise interval is then used as the end of the current emission interval and the beginning of the next one. The only case where an emission interval is terminated before another one starts is when the flux drops below zero. Then the interval is stopped, and the next interval starts at the rise front of the next trapezoid in the burst decomposition. This procedure generally isolates intervals where the flux has risen and fallen by a significant fraction of the peak flux during that interval. This requirement ensures that most of the flux present during the interval is due to peak emission primarily restricted to that interval. It is a reasonable method for isolating distinct emission intervals.

Figure 21 shows the results of this interval selection procedure applied to the example burst of this section. The trapezoidal decomposition is represented in physical units. The intervals are shown in ascending order across the flux history of the burst. All the burst's flux is contained within emission intervals with this particular procedure.

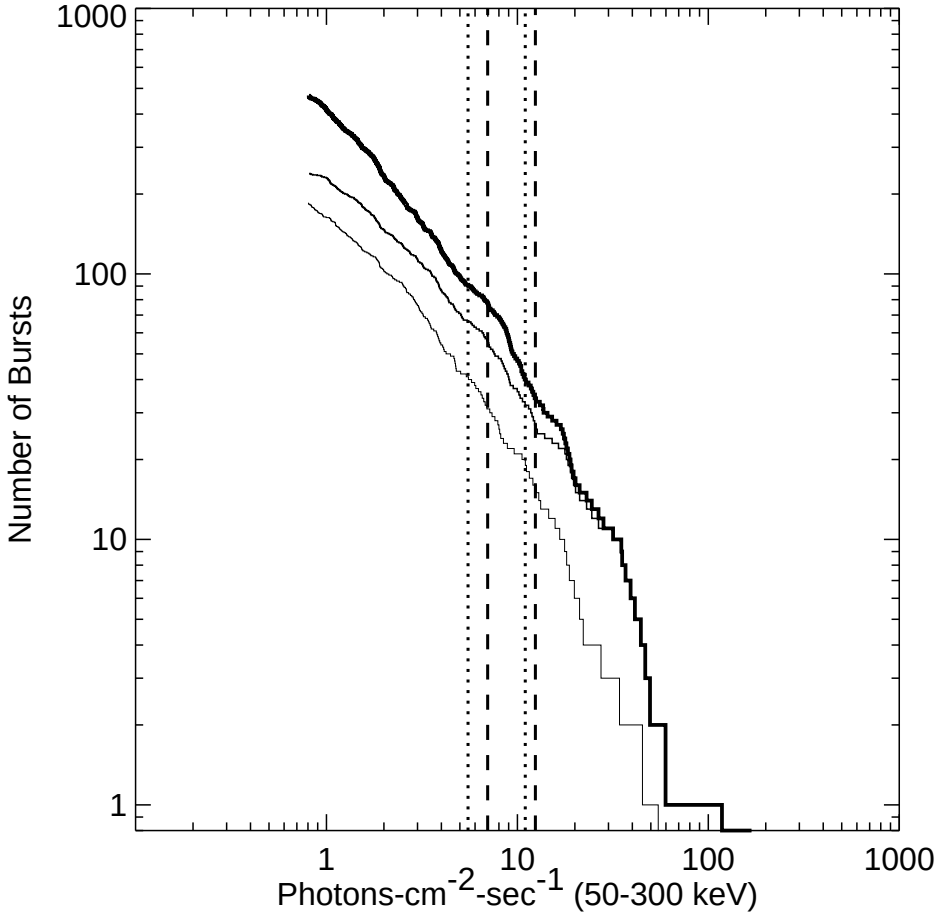

FIG. 23.—Peak flux intensity distributions on the 64 ms timescale for the data analyzed with the peak decomposition algorithm. *Upper thick-lined histogram:* All HE bursts. *Upper thin-lined histogram:* Multipeaked HE bursts. *Lower thin-lined histogram:* Second brightest peaks within HE bursts.

APPENDIX B

STUDY OF THE IMPACT OF SPECTRAL CONSTRAINTS ON THE PEAK FLUX CALCULATION ON BURST INTENSITY DISTRIBUTIONS

It is worthwhile verifying that selecting peaks in a constrained way, which may result in intensities other than the very brightest from a burst, can yield results other than homogeneous distributions. If picking some peak other than the brightest one always made the calculated peak flux much smaller, then we would expect that we could only see the brightest bursts this way and that the distributions would generally come out homogeneous, just like the brightest burst set. It should be pointed out here that the peak flux of the NHE peak from a HE burst is sometimes actually the brightest peak. However, since this is not usually the case, we have run some tests to study the peak flux selection effects.

We changed the peak interval section criterion from NHE peaks to peaks with 50–300 kev spectral indices in the range -3 to -1. This range brackets the NHE peak spectral index distribution in the 50–300 kev range, shown in the lower left-hand panel of Figure 15. The peak flux distribution that resulted when this selection criterion was applied to the HE burst data is shown as the lower thin histogram in Figure 22 and has $\langle V_p/V_{\rm plim}\rangle = 0.324 \pm 0.022$. This distribution is clearly very different from the NHE peak distribution. Also shown in this figure are the total and multipeaked HE burst distributions. The distribution selected here differs from the multipeaked distribution by 1.36 σ according to the $\langle V_p/V_{\rm plim}\rangle$ value. The intensity distribution break ranges for the multipeaked HE bursts (*dashed vertical lines*) and the other selected subset (*dotted vertical lines*) overlap and do not indicate that one set of peaks is intrinsically less luminous than the other.

We also tried calculating the peak flux distribution using the second brightest peak regardless of the spectral characteristics. This distribution is shown in Figure 23, and it has a $\langle V_p/V_{\rm plim}\rangle$ value of 0.317 ± 0.022. Also, the break ranges of the multipeaked HE bursts and this subset, marked as in Figure 22, overlap significantly. It is clear that simply selecting a peak flux other that the very brightest peak does not automatically result in a homogeneous distribution. These analyses indicate that the properties of the intensity distributions of the NHE peak fluxes from HE bursts should not be considered as artifacts of the peak selection methodology.

REFERENCES

Belli, M. 1995, Ap&SS, 231, 43
Davis, S., et al. 1994, in AIP Conf. Proc. 307, Proc. 2d Huntsville Workshop on Gamma-Ray Bursts, ed. G. J. Fishman, J. J. Brainerd, & K. Hurley (New York: AIP), 182
Fishman, G., et al. 1989, in Proc. GRO Science Workshop, ed. W. N. Johnson (Greenbelt:NASA/GSFC), 2-39
Fishman, G. J., et al. 1994, ApJS, 92, 229
Horack, J. M., & Emslie, A. G. 1994, ApJ, 428, 620
Koshut, T. M., Paciesas, W. S., Kouveliotou, C., Van Paradijs, J., Pendleton, G. N., Fishman, G. J., & Meegan, C. A. 1996, ApJ, 463, 570
Kouveliotou, C., et al. 1993, ApJ, 413, L101
———. 1996, in AIP Conf. Proc. 384, Proc. 3d Hunstville Workshop on Gamma-Ray Bursts, AIP, ed. C. Kouveliotou, M. S. Briggs, & G. J. Fishman (New York: AIP), 42
Lestrade, J., et al. 1994, in AIP Conf. Proc. 307, Proc. 2d Huntsville Workshop on Gamma-Ray Bursts, ed. G. J. Fishman, J. J. Brainerd, & K. Hurley (New York: AIP), 212
Meegan, et al. 1996, ApJS, 106, 65
Norris, et al. 1994, ApJ, 424, 540
Pendleton, G., et al. 1994, ApJ, 431, 416
———. 1995a, ApJ, 439, 963
———. 1995b, Nucl. Instrum. Methods Phys. Res A, 364, 567
———. 1996, ApJ, 464, 606
———. 1997, in preparation
Schmidt, M., Higdon, J., C. & Hueter, G. 1988, ApJ, 329, L85